

Convective hydration in the tropical tropopause layer during the StratoClim aircraft campaign: Pathway of an observed hydration patch

By K. O. Lee et al.

Reply to the co-editor's comments

In the following, the comments made by the referees appear in black, while our replies are in red, and the proposed modified text in the typescript is in blue.

Co-Editor comments

In general both reviewers point to the issue of numerical diffusion in the model. While I realise that you have already done work to address these comments, I would ask you to pay attention again to this point when revising your manuscript. Actually, as far as I can see, this point mainly refers to the employed tracer transport scheme, which is PPM (and again this point could be more clearly made). Long time ago, I looked at the issue of numerical diffusion in schemes including PPM (Müller, R., MWR, 1992, Vol 120., p. 1407); I actually think that you selected a scheme which really minimizes numerical diffusion, which you might want to emphasize in your manuscript.

Thank you for nice suggestion. As you mentioned, the employed tracer transport scheme, which is PPM (piecewise parabolic method), is accurate and sophisticated method to minimize the numerical diffusion (Muller, 1992). This tip of information has been included in the manuscript.

♣ Page 6, lines 146–147

"[...] while other variables are transported with the piecewise parabolic method (PPM) scheme (Colella and Woodward, 1984), a scheme with excellent mass-conservation properties and low numerical diffusion (Muller, 1992)."

♣ Page 11, line 290–291

"Note that the even low numerical diffusion of the PPM scheme also contributes to the dispersion of the hydration patch."

♣ Page 21, lines 605–607

Müller, R.: The performance of classical versus modern finite-volume advection schemes for atmospheric modelling in a one-dimensional test-bed, *Mon. Wea. Rev.*, 120, 1407–1415, [https://doi.org/10.1175/1520-0493\(1992\)120%3C1407:TPOCVM%3E2.0.CO;2](https://doi.org/10.1175/1520-0493(1992)120%3C1407:TPOCVM%3E2.0.CO;2), 1992.

Further, reviewer #1 pointed to the issue of the importance of "ice microphysics". You have now mentioned this point, but my recommendation is to be more specific; ice microphysics encompasses many processes. I think specifically in-situ ice nucleation and subsequent growth of the ice particles is meant here. I suggest to bring this issue across more clearly.

Right. As suggested the term of "ice microphysics" has been replaced or specified in the manuscript.

♣ Page 1, line 26

"ice nucleation and water vapour deposition."

♣ Page 16, line 439

"[...] The ice microphysics (e.g. nucleation, growth and sedimentation of ice particles) might play [...]"

♣ Page 35, lines 731–734

"[...] water vapour deposition followed by ice sedimentation [...]"

A final point: the paper should contain a "data availability" statement according to ACP recommendations.

The "data availability" statement has been included.

♣ Page 17, lines 485–487

Data availability

After the StratoClim embargo period, the aircraft data will be freely available. Meso-NH output data are available from JPC upon request.

Specific Comments:

Rev. #1

Figure A: I suggest you add this figure to the paper as an electronic supplement, extend the caption somewhat and provide a link to the supplement in the paper.

Thanks for nice suggestion. We isolate the Figure A in supplement file (supplement.pdf), linking to the part defining the "hydration patch" in section 2.3.

♣ Page 6, line 162–163

"[...] The hydration patch is chased visually back in time every hour from 06:00 UTC on 8 August to 13:00 UTC on 6 August 2017 (for more details, see Figure S1 in the Supplement) [...]"

p. 16, l. 459: change second line to: "allows the mixture of tropospheric and stratospheric air parcels in the TTL... overshoots to be understood..."

Corrected.

♣ Page 17, lines 473–474

"allows ~~to understand~~ the mixture of tropospheric and stratospheric air parcels in the TTL by vigorous convective overshoots to be understood."

p. 17, l. 463: "Sophisticated analyses": provide a bit more detail what sophisticated means here.

Corrected.

♣ Page 17, lines 474–475

"[...] To estimate the detailed origin i.e. defining the lower, middle, and upper troposphere, of air parcel, further analyses using passive tracers [...]"

p. 8, l. 224-228: "They overshoots"??

Corrected.

♣ Page 8, line 229

"[...] and they ~~overshoots~~ develop in this region [...]"

p. 16, l. 458-459: "sensitive": can you indicate how the amount changes is the grid spacing is changed (say increased)?

Added

♣ Page 17, lines 469–471

"[...] note that the amount of injected moisture is sensitive to the grid spacing of simulation (up to a factor of 3 with horizontal grid spacing varying from 1600 to 100 m; Dauhut et al., 2015) [...]"

p. 9, l. 253: "within the overshooting of the..." sentence is unclear.

Corrected.

♣ Page 9, line 260

"[...] as the ~~air within the overshooting of the~~ ice-laden air ~~within the convective overshoots~~ mixes with [...]"

p. 11., l. 301-311: "shortly" -> "on short time scales"

Corrected.

♣ Page 11, lines 316–317

"[...] occurs ~~on shortly~~ time scales within [...]"

p. 6., l. 164-167: "reduced by" --> "reduced to"

Corrected.

♣ Page 6, line 167

"[...] but it is reduced ~~to-by~~ one fourth [...]"

p. 14, l. 384-385: First, "thanks" should be changed to "due to", but the message is still not clear: why would mixing induce sedimentation? Please clarify/extend the discussion.

You are right. Indeed, sublimation is the process that reduces the ice content here.

♣ Page 14, lines 393–394

"[...] The reduced ice content in ML and IL might be induced by ~~sedimentation thanks to~~ sublimation due to the mixing with the dry tropospheric air [...]"

Figure 13: I am confused: the caption says now that the hatched area in (c) shows the layer of dehydration. But the hatched area in (c) overlaps with an area marked as "hydration". Isn't this a contradiction? Please clarify.

Right. The yellow capsule indicates the hydration patch, while the hatched area depicts the layer of dehydration. Because the hydration patch reduces with time, it is affected by dehydration. This explains the overlap of the hydration patch and the layer of dehydration. This schematic summarizes the vertical profile of water vapour mixing ration shown in Fig. 11d. For better understanding, the hatched area of dehydration has been little shifted toward down in Fig. 13c.

♣ Figure 13

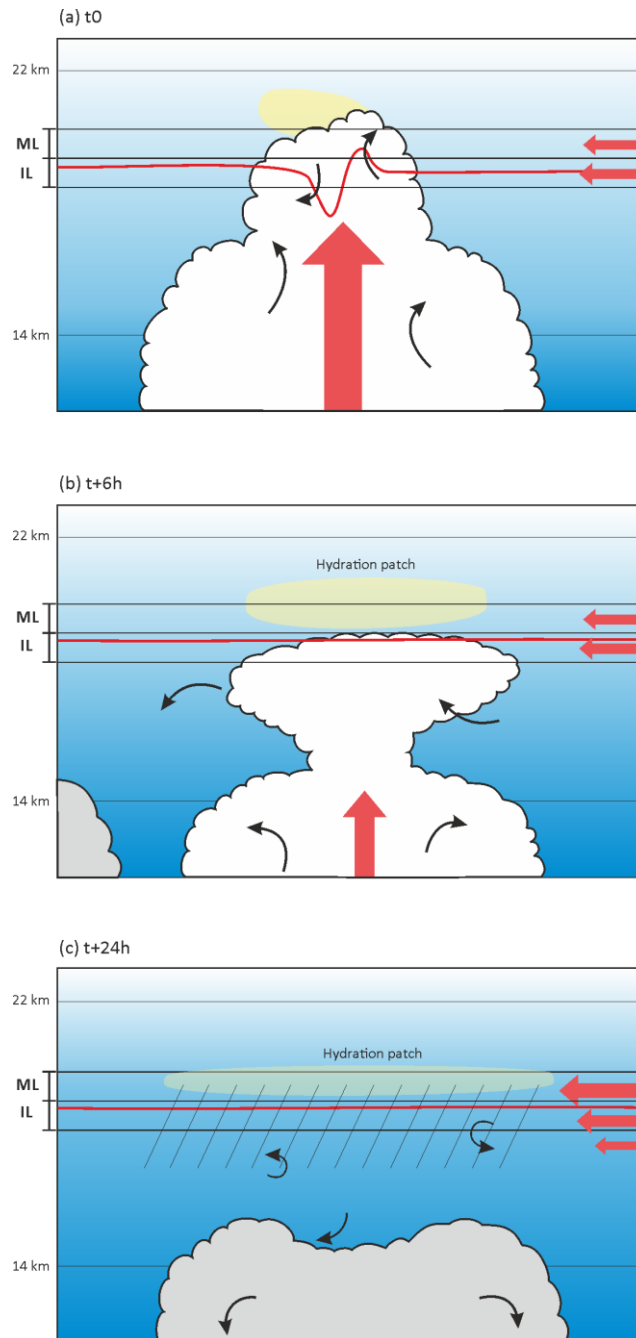


Figure 13. Schematic illustration summarising the hydration process in the TTL during flight #7 of the StratoClim 2017 field campaign. (a) Mixing of the overshoots with the stratospheric air, (b) and (c) turbulent mixing of the hydration patch with the tropospheric air by vertical wind shear. The bottom and top of the TTL, 14 and 22 km, and the moist layer (ML) and ice layer (IL) are represented by the black solid line, and the 410 K isentropic altitude is represented by the red solid line. The main force in the TTL is marked by bold red arrows, while the turbulent eddies in/around the developed and weakened overshoots are described by black arrows. The overreaching water vapour above the cloud top level is indicated by a yellow ellipsoid in (a). The hydration patch is yellow-encapsulated in (a) and (b), and the layer of dehydration by turbulent diffusion and [water vapour deposition followed by ice sedimentation-ice microphysics](#) is hatched in (c). The blue shades illustrate the concentration of tropospheric air, showing the increased tropospheric air in the TTL by the turbulent mixing in (b) and (c).

p. 16, l 441 remained --> remaining

Corrected.

♣ Page 16, line 454

“remaining horizontal [...]”

Rev. #3

p. 13, l 364-365: growth of what?

Corrected.

♣ Page 13, line 371

“[...] by ice nucleation and **particle** growth [...]”

Fig. 13: see above

Corrected as suggested in above comment.

p. 6, l. 160-164: east-northeasterlies: not clear to me

Corrected to “north-easterlies”.

Convective hydration in the tropical tropopause layer during the StratoClim aircraft campaign: Pathway of an observed hydration patch

By K. O. Lee et al.

Reply to the referees' comments

In the following, the comments made by the referees appear in black, while our replies are in red, and the proposed modified text in the typescript is in blue.

Referee #1 comments

General Comments

Overall, the authors have addressed my comments. I appreciate the added discussion (and references), which have improved this article. I think the article will be ready for publishing with some additional discussion on certain simulated features that are not fully explained (see below).

We appreciate the time and effort you put in this review as well your mindful comments on our paper. We have included further details about the simulation features in particular, about numerical diffusion. Replies to each comment are listed below.

The role of isolated overshoots in the simulated widespread mixing is still unclear. The use of TKE to show mixing is not compelling for the widespread signal, as it just looks like an overall lifting of the tropospheric heights at later times. The authors do show mixing at the location of the overshoot. But what is missing is any signal that shows that mixing traveling outwards from that overshoot location. How can you explain that isolated overshoots cause mixing to appear uniformly throughout an entire layer of the atmosphere? (Particularly figures 8 and 9, panels h-l.) It doesn't make physical sense. A sentence or two added to the article that acknowledges the role of numerical diffusion (not just physical) in some of the signal would be useful. And that this component of the simulated signal needs more investigation. A little more discussion will be particularly valuable for readers of your article that are not modeling experts.

The employed tracer transport scheme, which is PPM (piecewise parabolic method), is accurate and sophisticated method to minimize the numerical diffusion (Muller, 1992). This tip of information has been included in the manuscript.

♣ Page 6, lines 146–147

"[...] while other variables are transported with the piecewise parabolic method (PPM) scheme (Colella and Woodward, 1984), a scheme with excellent mass-conservation properties and low numerical diffusion (Muller, 1992)."

♣ Page 11, line 290–291

"Note that the even low numerical diffusion of the PPM scheme also contributes to the dispersion of the hydration patch."

♣ Page 21, lines 605–607

Müller, R.: The performance of classical versus modern finite-volume advection schemes for atmospheric modelling in a one-dimensional test-bed, *Mon. Wea. Rev.*, 120, 1407–1415, [https://doi.org/10.1175/1520-0493\(1992\)120%3C1407:TPOCVM%3E2.0.CO;2](https://doi.org/10.1175/1520-0493(1992)120%3C1407:TPOCVM%3E2.0.CO;2), 1992.

Minor Comments:

Line 172-173: WMO 1957 & Maddox and Mullendore 2018 are not in the reference list.

Indeed. These are now listed.

Maddox, E.M. and Mullendore, G. L.: Determination of Best Tropopause Definition for Convective Transport Studies. J. Atmos. Sci., 75, 3433–3446, <https://doi.org/10.1175/JAS-D-18-0032.1>, 2018.

WMO: Definition of the tropopause, WMO Bull., 6, 136, 1957.

1
2 Convective hydration in the tropical tropopause layer during the StratoClim aircraft campaign:

3 Pathway of an observed hydration patch

4
5 Keun-Ok Lee¹, Thibaut Dauhut¹, Jean-Pierre Chaboureau¹, Sergey Khaykin², Martina Krämer³ and

6 Christian Rolf³

7 ¹Laboratoire d'Aérodologie, Université de Toulouse, CNRS, UPS, Toulouse, France

8 ²LATMOS-IPSL, Université Versailles St-Quentin; Sorbonne Université, CNRS/INSU, Guyancourt, France

9 ³Institute for Energy and Climate Research – Stratosphere (IEK-7), Forschungszentrum Jülich, Jülich, Germany

10
11 ABSTRACT

12 The source and pathway of the hydration patch in the TTL (Tropical Tropopause Layer) that was measured
13 during the StratoClim field campaign during the Asian summer monsoon in 2017, and its connection to
14 convective overshoots are investigated. During flight #7, two remarkable layers are measured in the TTL
15 namely, (1) moist layer (ML) with water vapour content of 4.8–5.7 ppmv in altitudes of 18–19 km altitudes
16 in the lower stratosphere, and (2) ice layer (IL) with ice content up to 1.9 eq. ppmv in altitudes of 17–18 km
17 in the upper troposphere around 06:30 UTC on 8 August to the south of Kathmandu (Nepal). A Meso-NH
18 convection-permitting simulation succeeds in reproducing the characteristics of ML and IL. Through
19 analysis, we show that ML and IL are generated by convective overshoots that occurred over the Sichuan
20 basin about 1.5 day before. Overshooting clouds develop up to 19 km, hydrating the lower stratosphere of up
21 to 20 km with 6401 t of water vapour by a strong-to-moderate mixing of the updraughts with the
22 stratospheric air. A few hours after the initial overshooting phase, a hydration patch is generated, and a large
23 amount of water vapour (above 18 ppmv) remained at even higher altitudes up to 20.5 km while the anvil
24 cloud top descends to 18.5 km. At the same time, a great part of the hydrometeors falls shortly, and the water
25 vapour concentration in ML and IL decreases due to turbulent diffusion by mixing with the tropospheric air,
26 ~~ice nucleation, and water vapour deposition~~. As the hydration patch continues to travel toward the south of
27 Kathmandu, tropospheric tracer concentration increases up to ~30 and 70 % in ML and IL, respectively. The
28 air mass in the layers becomes gradually diffused and it has less and less water vapour and ice content by
29 mixing with the dry tropospheric air.

Supprimé: and in-situ ice microphysics (e.g.

Supprimé: particle growth

Supprimé:)

33

34

35 **1. Introduction**

36 The Asian summer monsoon anticyclone is one of the most pronounced circulation patterns in the Northern
37 Hemisphere, and it is a dominant climatological feature of the global circulation during boreal summer
38 (Mason and Anderson, 1963; Randel and Park, 2006). The monsoon circulation horizontally covers large
39 parts of southern Asia and the Middle East, and is located on the edge of the tropics and subtropics. It
40 consists of cyclonic flow and convergence in the lower troposphere together with strong anticyclonic
41 circulation and divergence in the upper troposphere. This circulation is coupled with persistent deep
42 convection over the south Asia region during summer (June to September) (Hoskins and Rodwell, 1995).
43 The monsoon tropopause is relatively high at about 4.2 ppmv; the upper tropospheric anticyclonic circulation
44 extends into the lower stratosphere spanning from around 300 hPa and 70 hPa, i.e. approximately the whole
45 upper troposphere and lower stratosphere (UTLS) (Highwood and Hoskins, 1998; Randel and Park, 2006).

46 Due to the strong dynamical signature in the UTLS, the influence of the monsoon is evident in
47 chemical constituents, i.e. water vapour is relatively high at about 4.2 ppmv (Wright et al., 2011), ozone is
48 relatively low (Randel et al., 2001), and methane, nitrogen oxides, and carbon monoxide are relatively high
49 (Park et al., 2004; Li et al., 2005). Especially, the water vapour in the UTLS is controlled by the troposphere-
50 to-stratosphere transport of moisture across the tropical tropopause layer (TTL, located between ~150 hPa
51 (355 K, 14 km) and ~70 hPa (425 K, 18.5 km); Fueglistaler et al., 2009; Rolf et al., 2018). It is mainly driven
52 by the large-scale cold point tropopause temperature field, but also processes involving convection, gravity
53 waves, and cirrus cloud microphysics that modulate TTL humidity.

54 Convective overshoots that penetrate the tropopause directly inject air and water into the stratosphere.
55 Fundamentally, convection arises from the temperature difference between a parcel of warm air and the
56 cooler air surrounding it. Warm air, which is less dense, i.e. more buoyant, rises through the atmospheric
57 column and adiabatically expands and cools. When the temperature of the rising air parcel has cooled
58 sufficiently, the water vapour it contains will begin to condense and release latent heat. If air parcels within
59 the convective core have enough upward momentum, they continue to rise beyond their equilibrium level of
60 zero buoyancy, and form overshoots. They eventually form an overshoot that penetrate into the lowermost
61 stratosphere by crossing the cold point tropopause. The convective overshoots have the potential to increase

62 the humidity in the stratosphere via rapid sublimation of convectively lofted ice and mixing with dry
63 stratospheric air. This has been demonstrated in previous studies in both modelling and measurement
64 (Dessler and Sherwood, 2004; Chaboureaud et al., 2007; Jensen et al., 2007; Homeyer et al., 2014; Khaykin
65 et al., 2016; Rysman et al., 2016; Homeyer et al., 2017; Smith et al., 2017; Dauhut et al., 2018; Funatsu et al.,
66 2018; among others). Even a small volume of tropospheric air can carry a significant quantity of water in the
67 condensed phase. Mixing of tropospheric air with the surrounding stratosphere, which is typically sub-
68 saturated, facilitates the rapid sublimation of lofted ice. Also, the origin of the injected water to the TTL has
69 been studied by backward trajectory analysis at global scale, and it was found that the convective sources are
70 generally higher over the continental part of the Asian monsoon region in comparison to other tropical
71 regions, with shorter transit times (Tzella and Legras, 2005; Tissier and Legras, 2016). However, the net
72 contribution of convective overshoots to stratospheric water vapour concentration is not well understood at
73 mesoscale and is not well represented in global models because of the small spatial scales (less than a few
74 kilometres) and short time scales (less than few hours) over which convection occurs.

75 The tropical aircraft campaign of the Stratospheric and upper tropospheric processes for better Climate
76 predictions (StratoClim, www.stratoclim.org) took place in summer 2017. It aimed to improve our
77 knowledge of the key processes, i.e. microphysical, chemical and dynamical processes, which determine the
78 composition of the UTLS, such as the formation, loss, and redistribution of chemical constituents (water
79 vapour, ozone, and aerosol). During the campaign, eight dedicated flights were successfully operated with
80 the objective of documenting the connection between the moisture plumes in the UTLS and the convective
81 sources from south Kathmandu, Nepal, during summer monsoon season.

82 Our study focuses on part of flight #7 to the south of Kathmandu measuring the stratospheric
83 hydration in the altitudes between 17 and 19 km. The objective of our work is to investigate the source and
84 pathway of the localized moisture in the TTL that was measured by aircraft in connection to a convective
85 overshoot. This is done using a combination of airborne and spaceborne observations as well as a
86 convection-permitting simulation performed with a fine resolution in the TTL.

87 A detailed description of the dataset is given in section 2. Section 3 presents the moistened TTL
88 signature captured by airborne and spaceborne observations and the numerical simulation. Section 4
89 demonstrates the convective origin of the enhanced moisture and shows its evolution along its path in the
90 lower stratosphere. A summary and discussion of the findings of the present study are given in section 5.

Code de champ modifié

91

92

93 **2. Data and method**

94 M55-Geophysica aircraft deployment in Kathmandu during Asian Summer Monsoon in July-August 2017
95 provided unprecedented sampling of the UTLS region above the southern slopes of Himalayas. More details
96 concerning the observational datasets used in this study together with the airborne and spaceborne
97 measurements and the convection-permitting simulation are provided in the following.

98

99 *2.1. StratoClim airborne observations*

100 During flight #7, the M55-Geophysica aircraft flew back and forth between Kathmandu in Nepal and west
101 Bengal in India (for the track, see the red line in Fig. 1) from 04:30 UTC to 06:50 UTC on 8 August 2017.
102 In-situ sensor onboard the aircraft measures the relative humidity with respect to ice (hereafter called simply
103 ‘relative humidity’ or ‘RH_{ice}’), temperature and wind speed and direction every 1 second. FLASH and FISH
104 instruments on board the Geophysica aircraft sampled the vertical water vapour and ice content distribution
105 every 1 second, respectively.

106 FLASH-A (Fluorescent Lyman-Alpha Stratospheric Hygrometer for Aircraft) is an advanced version
107 of the airborne FLASH instrument (Sitnikov et al, 2007; Khaykin et al., 2013) previously flown onboard the
108 M55-Geophysica aircraft. FLASH-A has a rear facing inlet allowing measurement of gas-phase water in the
109 altitude range between 12–21 km, with the latter being the aircraft ceiling altitude. Total uncertainty of water
110 vapour measurement amounts to 9 % with a detection limit of 0.2 ppmv, whereas the measurement precision
111 at 1 Hz sampling is better than 6 %.

112 FISH (Fast In situ Stratospheric Hygrometer) is a closed-path Lyman- α photo fragment fluorescence
113 hygrometer that measures total water (sum of gas phase and evaporated ice crystals) in the range of 1–1000
114 ppmv between 50 and 500 hPa levels with an accuracy and precision of 6–8 % and 0.3 ppmv (Zöger et al.,
115 1999; Meyer et al., 2015). The time resolution of the measurements is 1 Hz. Inside of ice clouds, ice water
116 content (IWC) is calculated by subtracting the gas phase water measured by FLASH from the total water
117 detected by FISH as described by Afchine et al. (2018). The minimum detectable IWC is 3×10^{-2} ppmv
118 ($\sim 3 \times 10^{-3}$ mg m⁻³).

119

120 *2.2. Spaceborne observation*

121 Calibrated thermal infrared brightness temperature (BT) data at 10.8 μm wavelength, acquired every 15 min
122 by the Spinning Enhanced Visible and Infrared Imager (SEVIRI) onboard the geostationary Meteosat Second
123 Generation satellite (MSG) were employed to investigate the evolution of deep convection. The spatial
124 resolution of the MSG-SEVIRI data used is 0.05° in both latitude and longitude. BT minima are generally
125 indicative of the cloud top overshoots associated with deep convection (e.g. Kato, 2006, Lee et al., 2016).

126 Vertical profiles of backscatter retrieved from the Cloud-Aerosol Lidar with Orthogonal Polarization
127 (CALIOP) on board CALIPSO (Winker et al. 2009) with a wavelength at 532 nm are used. CALIOP
128 provides observations of particles, including high clouds, with a very high sampling resolution, 30 and 335 m
129 in the vertical and horizontal directions, respectively.

130

131 *2.3. Cloud-resolving numerical simulation*

132 The target convective overshoots and the moistened TTL were simulated using the non-hydrostatic numerical
133 research model, Meso-NH (Lac et al. 2018). For a fine-scale analysis, the simulation uses about 400 million
134 grid points with horizontal grid spacing of 2.5 km. The vertical grid has 144 stretched levels (Gal-Chen and
135 Somerville, 1975) with a spacing of 250 m in the free troposphere and the stratosphere and a finer resolution
136 of 100 m close to the surface and between 16 and 19.5 km inside the TTL. The simulation domain covers
137 northern India and China (Fig. 1, 5000 km \times 3600 km) encompassing the track of flight #7 and the
138 overshooting clouds over the Sichuan basin. The simulation was initialized at 00:00 UTC on 6 August 2017
139 and the initial and lateral boundary conditions are provided by the operational European Centre for Medium-
140 Range Weather Forecasts (ECMWF) analyses every 6 hours. It ran for 3 days providing outputs every 1 hour.

141 The model employs a 1-moment bulk microphysical scheme (Pinty and Jabouille, 1998), which
142 governs the equations of six water categories (water vapour, cloud water, rainwater, pristine ice, snow and
143 graupel). For each particle type, the sizes follow a generalized Gamma distribution while power-law
144 relationships allow the mass and fall speed to be linked to the diameters. Except for cloud droplets, each
145 condensed water species has a nonzero fall speed. The turbulence parametrisation is based on a 1.5-order
146 closure (Cuxart et al., 2000) of the turbulent kinetic energy equation and uses the Bougeault and Lacarrere
147 (1989) mixing length. The transport scheme for momentum variables is the weighted essentially non-
148 oscillatory (WENO) scheme of 5th order (Shu and Osher, 1988) while other variables are transported with the

149 piecewise parabolic method (PPM) scheme (Colella and Woodward, 1984), [a scheme with excellent mass-](#)
150 [conservation properties and low numerical diffusion \(Muller, 1992\).](#)

Supprimé: which is

Supprimé: very accurate and sophisticated method to minimise the

151 To assess the simulation, airborne measurement data (along about 85.2°E, 25–26.5°N, blue line in Fig.
152 1) between 06:20 and 06:48 UTC on 8 August 2017 are compared to the simulation results averaged in a box
153 (85–85.5°E, 25–26.5°N, marked by ‘HYD’ in Fig. 1) at 06:00 UTC on the same day. The CALIOP
154 backscatter coefficients are compared to those simulated from the model outputs using the Meso-NH lidar
155 simulator, which takes into account all the predicted scattering particles (Chaboureau et al. 2011). The
156 SEVIRI/MSG BTs are compared to synthetic BTs computed offline using the Radiative Transfer for TIROS
157 Operational Vertical Sounder (RTTOV) code version 11.3 (Saunders et al. 2013) from the simulation outputs
158 (Chaboureau et al. 2008).

159 In this study, a ‘hydration patch’ is defined as a region with a water vapour amount larger than the
160 background value at 410 K isentropic level. The background equals 5.2 ppmv which corresponds to the water
161 vapour averaged in the box 74–84°E, 15–25°N (shown with dashed line in Fig. 1). Such a hydration patch is
162 located within the moist layer (ML) of 18–19 km altitude (see Figure 2), corresponding to an enhanced value
163 of water vapour observed during the last descending of flight #7 (see section 3.1). Below the hydration patch,
164 the ice layer (IL) is located between 17 and 18 km, where an increase of ice content is observed during the
165 same period. The hydration patch is chased visually back in time every hour from 06:00 UTC on 8 August to
166 13:00 UTC on 6 August 2017 ([for more details, see Figure S1 in the Supplement](#)), considering the prevailing
167 wind direction and speed at 410 K isentropic altitude. At 14:00 UTC, a large amount of water vapour (≥ 6.6
168 ppmv), that is injected by the convective overshoot in the Sichuan basin, starts to appear at this altitude,
169 generating a hydration patch. With the dominant [north-easterlies](#) ($15\text{--}20\text{ m s}^{-1}$), it travels to the south of
170 Kathmandu. The area of the hydration patch is about 6,000 km², but it is reduced [to](#) one fourth to about 1,500
171 km² during the initial overshooting phase in the convective region. This domain is used to calculate the
172 average values of water vapour, ice content, temperature, and relative humidity displayed in Figures 9, 10,
173 and 11.

Supprimé: east-

Supprimé: by

174 To understand the processes along the pathway of the hydration patch, four analysis times are selected:
175 1) a few hours before the overshoot development at 13:00 UTC on 6 August, 2) the overshoot development
176 time at 21:00 UTC on the same day, 3) a few hours after the overshoots at 12:00 UTC on 7 August, and 4)
177 the aircraft measurement time at 06:00 UTC on 8 August 2017. There exist several tropopause definitions,

183 considering temperature lapse rate, potential vorticity, and static stability (WMO, 1957; Maddox and
184 Mullendore, 2018). In this study, the overshoots are defined as convective cloud tops that reach the
185 lowermost stratosphere above 380 K level. This simple definition is sufficient enough to study the impact of
186 convective hydration on the TTL as it quickly returns to its undisturbed state (Dauhut et al., 2018). A tracer
187 of tropospheric air is also calculated on line during the Meso-NH run. At the simulation initiation, the
188 tropospheric and stratospheric air masses are divided by a boundary at 380 K level, and the tracer values are
189 set to 1 and 0 below and above, respectively. In other words, pure concentration of tropospheric
190 (stratospheric) air has tracer value equal to 100 (0) %.

191

192 **3. Convective hydration in the TTL**

193 *3.1. Moistened layers in the TTL*

194 FISH and FLASH instruments on board flight #7 measure moisture and ice content in the TTL to the south of
195 Kathmandu along the track of $\sim 85.2^\circ\text{E}$, $25\text{--}26.5^\circ\text{N}$ (blue line in Fig. 1) from 06:20 to 06:48 UTC on 8
196 August 2017. ML and IL were observed. ML is evident at altitudes of 18–19 km by the water vapour content
197 of 4.8–5.7 ppmv (solid line in Fig. 2a), and IL is apparent at altitudes of 17–18 km with the ice content of up
198 to 1.9 eq. ppmv (solid line in Fig. 2b) and water vapour of 3.3–5.0 ppmv (solid line in Fig. 2a). The
199 temperature minimum, which defines the cold point tropopause (CPT, red line in Fig. 2c), equals -83.5°C at
200 17.8 km in between ML and IL (black line in Fig. 2c). In ML, the potential temperature ranges between 394
201 and 428 K, while in IL it ranges between 372 and 393 K (blue line in Fig. 2c). Figure 2d shows that RH_{ice}
202 increases beyond 70 % in ML and IL, and that IL is partly super-saturated with RH_{ice} up to 118 %. In both
203 ML and IL, strong easterly wind prevails (black line in Fig. 2e) with wind speed exceeding 20 m s^{-1} (blue
204 line in Fig. 2e), while easterlies stronger than 30 m s^{-1} are seen at 17 and 18.5 km altitudes.

205 Figure 2 also evidences that Meso-NH succeeds in reproducing most of the measurements in the TTL.
206 It reproduces the enhanced amount of water vapour in both ML and IL. In ML, the simulated water vapour in
207 the range between 4.9–6.0 ppmv with an average value (black cross marks in Fig. 2a) of 5.5 ppmv
208 reproduces the measured 4.2–5.6 ppmv well. In IL, the appearance of ice (black cross marks in Fig. 2b) is
209 simulated, but with a maximum value of 0.65 eq. ppmv, a factor of 3 less compared to the measured
210 concentrations. The simulation captures well the CPT at 17.8 km altitude and -83.3°C (cross marks in Fig.

211 2c), RH_{ice} values of 70–100 % between 16.5–18.5-km altitudes (cross marks in Fig. 2d), and the strong
212 easterly wind (black and blue cross marks in Fig. 2e). Despite small vertical variations in water vapour and
213 temperature that are missing around the CPT, the simulation is good enough to being used to investigate the
214 source and the pathways of water in ML and IL.

215 A few hours before the Geophysica measurements and upstream, some clouds were observed in the
216 TTL by CALIOP around 20:00 UTC on 7 August 2017. Figure 3a shows a V-shaped region of strong
217 backscatter values of $0.001\text{--}0.008\text{ km}^{-1}\text{ sr}^{-1}$ from 15 to 18.5 km altitudes over India along the track of
218 $25.5\text{--}31.5^\circ\text{N}$ (yellow line in Fig. 1). The V-shaped strong backscatter region is successfully reproduced by
219 Meso-NH (Fig. 3b) at 15–18.5-km altitudes between 26.5 and 31°N but with backscatter values lower than
220 measured. The simulated V-shaped region is characterized by low ice content ($\geq 0.1\text{ eq. ppmv}$, Fig. 3c) while
221 an above-background amount of water vapour of 5–7 ppmv is layered at altitudes higher than 18 km, (Fig.
222 3d), where ML is located. The V-shaped strong backscatter region is possibly induced by waves propagating
223 at these high altitudes, e.g. gravity waves. Investigating the mechanism at its origin is however beyond the
224 scope of this article. It is worth noting that the above-background water vapour concentration and the ice
225 content are already upstream ($93\text{--}95^\circ\text{E}$) about 10 hours before flight #7 ($\sim 85.2^\circ\text{E}$) and that Meso-NH is able
226 to resolve clouds in the UTLS.

227

228 3.2. Target convective overshoots

229 In the region where ML and IL are located, the simulated hydration patch (water vapour $\geq 5.2\text{ ppmv}$) is in
230 evidence at the 410 K level at 06:00 UTC on 8 August 2017 (Fig. 4a). It is positioned above high-level
231 clouds, as shown with BT values lower than -47°C in both the SEVIRI/MSG imagery and the Meso-NH
232 simulation in Fig. 5a and 5b (pointed by arrows), respectively. This hydration patch has been advected from
233 the east by the strong easterlies (about 25 m s^{-1} , see Fig. 2e). At 12:00 UTC on 7 August, it is located around
234 eastern India (Fig. 4c) and is associated with low BT values ($\leq -55^\circ\text{C}$) in both the MSG/SEVIRI imagery
235 (pointed by an arrow in Fig. 5c) and the Meso-NH simulation (Fig. 5d). This suggests that the hydration
236 patch is generated by the injection of water by convective overshoots. The convective overshoots start to be
237 seen from 14:00 UTC on 6 August over the Sichuan basin (Fig. 4e), and they develop in this region until
238 21:00 UTC. During the period between 14:00 and 21:00 UTC, the developing overshoots collectively inject a
239 large water vapour hourly budget of 896 t above the CPT (as the result of integrating the water vapour

Supprimé: overshoots

241 content between two isentropic altitudes of 380 and 530 K). The signature of overshoots is evidenced over
242 the Sichuan basin at 21:00 UTC by the large amount of water vapour in excess of 18 ppmv at 410 K level
243 (Fig. 4d) and by BT values lower than -80°C (Fig. 5e and 5f). At 13:00 UTC before the overshoot
244 development, neither water vapour mixing ratio larger than 5 ppmv nor BT values lower than -60°C are
245 distinguishable over the Sichuan basin (box in Fig. 5g and 5h).

246 In summary, a good agreement is achieved between the measurements (airborne and spaceborne) and
247 the Meso-NH simulation. The analysis of the simulation shows that the water-enhanced layers in ML and IL
248 observed to the south of Kathmandu around 06:30 UTC on 8 August were generated by the injection of water
249 by the convective overshoots produced over the Sichuan basin during 14:00–21:00 UTC on 6 August.

250

251 **4. Pathway of the hydration patch and processes affecting it**

252 *4.1. Evolution of the hydration patch during its way to the south of Kathmandu*

253 The hydration patch is described along its way from the Sichuan basin to the south of Kathmandu. In the
254 following, vertical sections of water vapour, ice content and tropospheric tracer are shown across the
255 hydration patch in the west-east orientation every 2 to 6 h (Figs. 6, 7, and 8). The vertical cross-sections are
256 centred over the hydration patch, all with the same size.

257

258 *4.1.1. Injection of water into the TTL by convective overshoots*

259 The vertical cross-sections of water vapour and ice content evidence that the large amounts of water vapour
260 and ice are injected above 380 K level by the convective overshoots that occurred during 15:00–21:00 UTC
261 on 6 August. At 13:00 UTC (Fig. 6a), just before the overshoot development, a strong upward motion is seen
262 at 16–18-km altitudes, while the cloud top (black solid line) is located in IL (about 17.5 km), just below the
263 CPT. At 15:00 UTC (Fig. 6b), a large amount of water vapour (≥ 15 ppmv) is in evidence in ML above 410
264 K level while a large ice content in excess of 120 eq. ppmv is found in IL, between 380 and 410 K levels
265 (Fig. 7b). Figure 8a–b shows that during 15:00–17:00 UTC the concentration of the tropospheric tracer
266 increases in both ML and IL with values of 4 and 30 %, respectively.

267 At 17:00 UTC and even higher cloud top is apparent at ~ 19.5 km altitude (Fig. 6c), a large amount of
268 water vapour (≥ 18 ppmv) rises to ~ 20 km, around 103°E , and a large ice content (≥ 120 eq. ppmv) stays
269 below 18 km altitude (Fig. 7c). The large amount of water is directly injected by convective overshoots

270 mainly in the form of ice, as the ice-laden air within the convective overshoots mixes with the entrained
271 stratospheric air during the collapse of the overshooting top. The warm, sub-saturated stratospheric air causes
272 the ice to rapidly sublimate into water vapour at the top of the overshoot, moistening the layer. It is worth
273 noting the water injected by the convective overshoots at 15:00 UTC is still apparent in ML at 17:00 UTC
274 around 102°E with a water vapour mixing ratio above 9 ppmv (Fig. 6c). In a similar way, the convectively-
275 injected large moisture at 17:00 UTC around 103°E (Fig. 6c) is found in ML at 19:00 UTC around 102.5°E
276 with a water vapour mixing ratio larger than 15 ppmv (Fig. 6d). At 19:00 UTC (Fig. 6d), the strong
277 convective updraughts perturb the isentropic surfaces (red solid lines), descending the 410 K level largely
278 from about 18.5 to 17.5 km. At 21:00 UTC a higher cloud top is found above ML in a wide area
279 (102.3–103.3°E longitude). The injected water vapour (≥ 18 ppmv) is transported above 20.5 km (Fig. 6e)
280 while the concentration of 0.1–0.5 % of the tropospheric tracer is seen in the water vapour pocket. The large
281 ice content exceeding 120 eq. ppmv is distributed mostly in IL (Fig. 7e). During 15:00–21:00 UTC (Fig.
282 8b–e), a concentration of 2–20 % of the tropospheric tracer is consistently seen in ML, while higher
283 concentration of 40 % has been found in IL. During 17:00–21:00 UTC (Fig. 9c–e), the large turbulent
284 kinetic energy (TKE) of 0.2–0.9 $\text{m}^2 \text{s}^{-2}$ is apparent in a limited area of cloud top (~103°E).

285 4.1.2. Evolution of the hydration patch along its pathway

286 From 23:00 UTC on 6 August to 06:00 UTC on 8 August 2017, the convective overshoots gradually
287 diminish in the region of longitude ~98–85°E and latitude ~28–25°N (see Fig. 4). At 23:00 and 00:00 UTC,
288 the anvil-shaped cloud above 16 km altitude presents a rather flat cloud top around 19 km (Fig. 7f and 7g).
289 The injected large amount of water vapour ≥ 18 ppmv is evident in ML, even at higher altitudes up to 20.5
290 km (Fig. 6f and 6g) whereas the large ice content ≥ 120 eq. ppmv is no longer apparent in IL (Fig. 7f and 7g).
291 Within the anvil cloud, still large TKE of 0.2–0.9 $\text{m}^2 \text{s}^{-2}$ is seen (Fig. 9f, g). During 06:00–18:00 UTC on 7
292 August, the water vapour mixing ratio in ML gradually decreases from 15 to ~9 ppmv, meanwhile the air
293 mass in IL becomes dry with a water vapour mixing ratio below 4 ppmv (Fig. 6h–j). During the same period,
294 the increase of tropospheric tracer concentration and TKE are evident in both ML and IL. The air mass with
295 concentration higher than 40 % is apparent in IL while the air mass with a lower tropospheric concentration
296 around 0.02–0.3 is seen in IL (Fig. 8h–j).

297 The air mass with high tropospheric tracer concentration of 2–40 % consistently exists in ML and IL
298 from 00:00 to 06:00 UTC on 8 August 2017 (Fig. 8k–l), while the TKE of 0.2–0.9 $\text{m}^2 \text{s}^{-2}$ exists in wide area

Supprimé: air within the overshooting of the

300 between the altitudes of 16 and 18 km (Fig. 9k–l). During this period, the hydration patch is further narrowed
301 and widened in ML (Fig. 6k–l), and the air mass becomes drier in IL (≤ 3 ppmv). [Note that the even low](#)
302 [numerical diffusion of the PPM scheme also contributes to the dispersion of the hydration patch.](#) At 00:00
303 UTC (Fig. 7k), new convection tops are apparent in altitudes of 16–17 km, and an increase of ice content
304 above 3 eq. ppmv is seen in IL. Then a decrease of ice content down to 0.1–1 eq. ppmv distributes in IL at
305 06:00 UTC where large ice content around 1–1.9 eq. ppmv was measured (see Fig. 2b).

306

307 *4.2. Processes affecting the hydration patch*

308 The processes that affect the moist and ice layers are further described. To this objective, average quantities
309 are calculated in ML and IL. The hourly evolution of water vapour, ice content, temperature, and RH_{ice}
310 shows the lifetime of the injected water in ML and IL along the pathway of the hydration patch (Fig. 10). The
311 profiles of tropospheric tracer, temperature, RH_{ice} , water vapour, ice content and wind speed give a vertical
312 view in the column across the tropical tropopause layer (Fig. 11). A scatter plot using tropospheric tracer and
313 water vapour highlights the mixing processes occurring in the hydration patch (Fig. 12).

314

315 *4.2.1. Mixing of the overshoots with the stratospheric air*

316 The hourly evolution of the average water vapour and the ice content along the pathway of the hydrated layer
317 demonstrates the hydration in the TTL by the convective overshoots (Fig. 10). During the development of the
318 convective overshoots between 14:00 and 21:00 UTC on 6 August 2017, the average water vapour mixing
319 ratio increases to 5.7 ppmv in IL (yellow solid line, Fig. 10a), while a large mixing ratio of 6.5 ppmv is seen
320 in ML (blue solid line in Fig. 10a). The ice content reaches more than 200 eq. ppmv in both layers and more
321 than 300 eq. ppmv in IL (Fig. 10b). Until 17:00 UTC, the temperature increases in both layers (solid lines in
322 Fig. 10c), indicating the mixing with the warmer stratospheric air. Because of this entrained stratospheric air,
323 RH_{ice} decreases largely below 60 % in ML (blue line with symbols in Fig. 10c), and down to 90 % in IL
324 (yellow line with symbols). Due to the mixing with entrained warmer stratospheric air, the enriched water
325 vapour layer then remains at this higher isentropic level after the overshoot collapses. The conditions and
326 timescale of the detailed process trapping the enriched water vapour in the TTL was demonstrated by Dauhut
327 et al. (2018). Thanks to a fine temporal resolution of 1 min, they revealed that this process occurs on short
328 time scales within 20 min. The active mixing of the convective overshoots with the stratospheric air between

Supprimé: ly

330 14:00 and 21:00 UTC is also evidenced by the evolution of vertical profiles of tropospheric tracer (Fig. 11a).
331 The tropospheric tracer concentration increases from 0 to 5 % in ML (yellow to green lines in Fig. 11a),
332 while the stratospheric air concentration (1 minus tracer) increases of 5 % in IL. The temperature increases in
333 both ML and IL (yellow to green lines in Fig. 11b) where the relative humidity decreases (yellow to green
334 lines in Fig. 11c).

335 The scatter plot of the tropospheric tracer and water vapour mixing ratio (Fig. 12) evidences the large
336 mixing of tropospheric and stratospheric air masses in the TTL (14–22 km altitudes). A large evolution of the
337 tropospheric tracer–water vapour diagram is found from 13:00 to 21:00 UTC on 6 August (Fig. 12a and
338 12b). At 13:00 UTC before the development of the convective overshoots, the air mass with potential
339 temperature (θ) of 410–420 K (yellow dots), corresponding to ML, is relatively dry with a water vapour
340 mixing ratio of 5–7.2 ppmv (Fig. 12a) and very small compounds of tropospheric air (tracer ≤ 0.1 %). The
341 air mass with θ of 380–390 K (black dots), corresponding to IL, has a low water vapour mixing ratio of
342 3–7.5 ppmv. At 21:00 UTC (Fig. 12b), the air mass with θ between 410 and 420 K becomes very humid
343 (5.5–13.6 ppmv of water vapour) and the concentration of tropospheric tracer increases to 0.2–8 %.
344 Moreover the air mass with very-high θ of 450–460 K (purple dots) is moistened largely as shown by a water
345 vapour mixing ratio above 15 ppmv. So does the air mass with θ between 390 and 410 K, which is both
346 moistened and enriched by the tropospheric tracer with a concentration of 5–60 % (red to orange dots, Fig.
347 12b). The convective overshoots also impact the air mass below the CPT by widening the range of the water
348 vapour mixing ratio with θ between 370 and 380 K (grey dots in Fig. 12a and b) from 3.2–13.9 ppmv at
349 13:00 UTC (Fig. 12a) to 0–18.8 ppmv at 21:00 UTC (Fig 12b).

350 From 17:00 UTC on 6 August to 02:00 UTC on 7 August, Fig. 9c shows that the temperature
351 decreases gradually (solid lines), while the relative humidity increases (lines with symbols). In ML and IL, a
352 great part of ice contents, especially snow and graupel fall quickly (dashed line in Fig. 10b), and the rest
353 sublimates. Meanwhile ice sediment out, still there is a low concentration of cloud ice in both ML and IL,
354 and the water vapour concentration slightly decreases (blue solid line in Fig. 10a). The continued presence of
355 cloud ice in ML suggests that the ice may have formed in-situ in response to wave-driven temperature
356 oscillations that locally drive the RH to ice saturation. The ice microphysics might play a pivotal role in
357 controlling the eventual moisture content since ice nucleation and the subsequent ice-growth process to
358 deplete slowly the ML. In ML, the relative humidity increases (in range of 65–80 %) mainly due to the

Supprimé: ¶

360 temperature decrease (in range of -78 and -82°C) (solid lines, Fig. 10c). During this period, the easterly
361 wind is nearly constant with the relatively-weak speed of $\sim 15\text{ m s}^{-1}$ in ML and $\sim 16.5\text{ m s}^{-1}$ in IL (yellow to
362 green lines, Fig. 11f). After 7 August, in ML, the relative humidity less than 80 % indicates strong sub-
363 saturation where a very small amount (0.1–0.3 eq. ppmv) of cloud ice still resides. This is probably induced
364 by the domain-averaged analysis.

365

366 4.2.2. Processes occurring in the hydration patch during the advection

367 After the development of the convective overshoots, the hydration patch travels westward across India and
368 north Bangladesh from 21:00 UTC on 6 August to 06:00 UTC on 8 August (Fig. 4). During its travel, the air
369 mass in ML and IL has less and less amount of water vapour and ice content (Fig. 10a–b).

370 Between 21:00 UTC on 6 August and 12:00 UTC on 7 August, the concentration of tropospheric tracer
371 increases at high altitudes with θ between 410 and 420 K up to 18 % (yellow dots, Fig. 12b–c). At the same
372 time, the water vapour decreases by a factor of two, in the range of 5–9.6 ppmv. This can be also seen in the
373 vertical profiles for which the concentration of tropospheric tracer increases at 12:00 UTC on 7 August in
374 both ML and IL (green to blue lines, Fig. 11a) and the water vapour decreases (green to blue lines, Fig. 11d).
375 The two layers become colder by $\sim 3^{\circ}\text{C}$ (green to blue lines in Fig. 11b), and dehydrated compared to the
376 initial state of 13:00 UTC on 6 August (yellow line in Fig. 11d, e). It includes much reduced amount of ice
377 content (green to blue solid lines in Fig. 11e), but still there exist ice content ≥ 1 eq. ppmv and cloud ice \geq
378 0.5 eq. ppmv at 12:00 UTC on 7 August (blue dashed line, Fig. 11e). In IL (Fig. 10c), RH_{ice} oscillates mostly
379 driven by temperature variation. Over time, the air mass in ML and IL gets colder and less humid by the
380 lowered cloud top below 17 km altitude. In both ML and IL, the easterly winds weaken below 15 m s^{-1} .
381 Moreover, the turbulent kinetic energy (TKE) increases from $0.1\text{--}0.3\text{ m}^2\text{ s}^{-2}$ at 21:00 UTC to $0.2\text{--}0.9\text{ m}^2\text{ s}^{-2}$
382 at 12:00 UTC in ML and IL (Fig. 9e, i). These results suggest that the water vapour concentration in ML and
383 IL decreases due to the turbulent diffusion in both the vertical and the horizontal direction consistent with the
384 increase of tropospheric tracer. Also, the vapour-scavenging effect by ice nucleation and particle growth
385 within IL contributes to reduce the water vapour deriving the dehydration. The rapid decrease of ice content
386 in IL due to both sublimation and sedimentation (Fig. 7f–i) results in the lowering of the cloud top from 17
387 to below 16 km at $97\text{--}101^{\circ}\text{E}$ at 06:00 UTC (Fig. 7h), and finally to 15 km around 95.5°E at 12:00 UTC (Fig.
388 7i).

389 Further increased tropospheric tracer concentration is distinguished from 12:00 UTC on 7 August to
390 06:00 UTC on 8 August 2017 in ML and IL (blue to red lines, Fig. 11a). Moreover the tropospheric tracer
391 concentration reaches to about 30 and 70 % in ML and IL, respectively while the water vapour decreases
392 (Fig. 11a and 11d). During this time, the cloud top height of convective cloud descends below 14 km (Fig.
393 6i–l), where RH_{ice} dramatically decreases (Figs. 2d, 11c). The entrained cold tropospheric air (and/or colder
394 background air) and the hydrostatic adjustment decrease the temperature in ML and IL (Fig.11b). It is worth
395 noting the shape of the temperature profile that becomes straight upward in the altitudes of 17–18.5 km
396 during the overshoot activity (green line, Fig. 11b). Also it is worth noting the decrease of ice content less
397 than 0.3 eq. ppmv (blue to red line, Fig. 11e), and the large-decrease of relative humidity in altitudes below
398 17.5 km.

399 The increased tropospheric tracer concentration in ML and IL is as well seen by the tracer–vapour
400 diagram of Fig. 12c–d. The concentration of tropospheric tracer increases at high altitudes with θ between
401 410 and 420 K (yellow dots) up to 20 % at 06:00 UTC on 8 August 2017, meanwhile the tropospheric air
402 concentration increases up to 50 % at the altitudes with θ between 390 and 400 K (red dots in Fig. 12d).
403 During the period (12:00 UTC on 7 August to 06:00 UTC on 8 August), the water vapour decreases in all
404 altitudes with θ above 380 K (Fig. 12c–d). It decreases from 9.6 to below 6.2 ppmv in ML (θ between
405 410–430 K, yellow and green dots) while dropping below 5 ppmv in IL (θ between 380–400 K, red and
406 black dots). The reduced ice content in ML and IL might be induced by sublimation due to the mixing with
407 the dry tropospheric air ($RH_{ice} \sim 50\text{--}70\%$) of below 16 km level (red line in Fig. 11c and cross marks in Fig.
408 2d). The air mixing of tropospheric and stratospheric air masses might be induced by the vertical wind shear
409 with the maxima wind speeds in excess of 30 m s^{-1} at ~ 17 and 18.5 km altitudes (see Fig. 2e, average value
410 in range of 18 and 25 m s^{-1} of red line in Fig. 11f). With the strengthened easterlies, the air mass in IL is well
411 mixed rather than conserved in this layer. Also, this wind shear layer with a large gradient of wind speed
412 ($25\text{--}35\text{ m s}^{-1}$) locates below and above the CPT (Fig. 2c, 2e), thus it results in the strait upward temperature
413 profile with the constant value about -80°C at 06:00 UTC on 8 August as seen in Fig. 10b (red line). The air
414 mass in ML and IL has large TKE values of $0.5\text{ m}^2\text{ s}^{-2}$ (Fig. 9l).

415

416 5. Conclusions

417 The source and pathway of the hydration patch in the TTL (Tropical Tropopause Layer) that was measured

Supprimé: sedimentation thanks to

Supprimé:

420 during flight #7 of the StratoClim 2017 field campaign during the Asian summer monsoon, and its
421 connection to overshooting convection are investigated. During the Geophysica flight #7 around 06:30 UTC
422 on 8 August 2017, two remarkable layers were observed to the south of Kathmandu above and below the
423 CPT located at 17.8 km, a moist layer (ML) with large water vapour content of 4.2–5.6 ppmv in altitudes of
424 18–19 km in the lower stratosphere, and an ice layer (IL) with large ice content up to 1.9 eq. ppmv at
425 altitudes of 17–18 km in the upper troposphere. The Meso-NH numerical simulation run with a 2.5 km
426 horizontal grid spacing succeeds in reproducing ML and IL. Through analysis using airborne and spaceborne
427 measurements and the numerical simulation, we show that the measured hydration patch in ML found in the
428 south of Kathmandu (~85°E) was produced by the convective overshoots that occurred over the Sichuan
429 basin (~103°E) between 14:00 and 21:00 UTC on 6 August 2017. The key hydration processes are
430 summarized schematically in Fig. 13.

431 The convective overshoots develop up to 19.5 km altitude in the Sichuan basin, and transport large
432 amount of water vapour of 6.5 ppmv to ML and ice content in excess of 300 eq. ppmv to IL. Between 15:00
433 and 21:00 UTC, the overshooting clouds collectively hydrate the lower stratosphere resulting in the total
434 amount of water vapour of 6088 t. It is also worth noting the large concentration of water vapour of over 18
435 ppmv up to 20 km level which is above the convective cloud top of 19.5 km (a yellow ellipsoid in Fig. 13a).
436 This feature is similarly seen during the development of the Hector the Convecton in the Tiwi Islands
437 (Dauhut et al., 2018), however, the magnitude is ~10 ppmv higher in the present event. The concentration of
438 the tropospheric tracer reaches to 8 and ~60 % in ML and IL, respectively, indicating the strong mixing of
439 the convective updraughts with the stratospheric air (black arrows in Fig. 13a). The strong convective
440 updraughts perturb the isentropic surfaces (red line in Fig. 13a), descending the 410 K level from 18.5 to
441 17.5 km. During these convective events, the mixing of the tropospheric and stratospheric air masses
442 increases the temperature in ML and IL. Moreover, the moderate -not intense- easterly wind (~15 m s⁻¹)
443 prevails constantly in these levels, and it does not interrupt the convection developing vigorously in altitude
444 (19.5 km ASL) and reaching the lower stratosphere.

445 The injected water by the convective overshoots generates the hydration patch, i.e. large water vapour
446 in ML (ellipse in Fig. 13b). During its westward travel, its altitude is kept constant by the moderate easterlies
447 of about 15 m s⁻¹ in ML and IL. The tropospheric tracer concentration is continuously increased in these
448 layers, where the above-background amount of water vapour is still remained and where the ice content

449 gradually sediments out and forms again along the pathway. It is highlighted that the large transported
450 amount of water vapour (≥ 18 ppmv) still remains at high altitudes of up to 20.5 km even when the anvil
451 cloud top descends to 18.5 km. Later on, the cloud top is still seen around 16–17 km level, keeping the large
452 RH_{ice} (about 95 %) in these altitudes. A part of the water vapour has been lost due to ice formation and
453 sedimentation and the turbulent diffusion in both vertical and the horizontal direction (black arrows in Fig.
454 13b). The ice microphysics (e.g. nucleation, growth, and sedimentation of ice particles) might play a pivotal
455 role in controlling the eventual moisture content since ice nucleation and the subsequent growth process
456 would slowly deplete the water vapour. This falling of ice and a reduced updraught are evident by the
457 lowered cloud top height partly from 17 to ~15 km (Fig. 13c).

458 Then the hydration patch continues to travel to the south of Kathmandu, with even higher tropospheric
459 tracer concentration of ~30 and 70 % in ML and IL, respectively (darkened blue shades in Fig. 13c). During
460 the same period, the top of convective clouds further descends below 14 km, thus the layer below IL, i.e.
461 15–17 km, becomes dry with RH_{ice} below 70 %. Due to mixing with the dry tropospheric air, the remaining
462 water vapour in ML gradually diffused in horizontal and vertical direction (ellipse). It is also true that the ice
463 content in IL is locally influenced by new convection with cloud top in altitudes 16–17 km about 6 h before
464 flight #7. The continuous air mixing might be induced by the vertical wind shear in altitudes 15–19 km
465 where the wind speed varies from ~18 to 25 m s⁻¹ (red bold arrows in Fig. 13c). The vertical mixing due to
466 wind shear modifies the temperature profile to the straight-upward in 17–18 km rather than bending. Also,
467 vertical motions caused by gravity waves breaking might play an important role in the transport of
468 tropospheric air into the TTL. In addition, after the strong updraughts of overshooting convection, the
469 remain~~ing~~ horizontal divergence in the lower stratosphere might let the tropospheric air continues to ascend.

470 Many of previous Lagrangian studies (Tzella and Legras, 2011; Tissier and Legras, 2016)
471 demonstrated the link between the moistened TTL and remote overshoots using large-scale numerical
472 simulations. Thanks to the combination of aircraft measurement and a 3-day convection-permitting
473 simulation, this study shed light on the processes along the pathway of a hydration patch from overshooting
474 clouds for 1.5 days, showing the 3-D evolution of water vapour and ice content.

475 This study focuses on the hydration patch that was measured during the last descending of flight #7
476 and the corresponding convective overshoots over the Sichuan basin. Here, the average water vapour amount
477 in the lower stratosphere is 6.5 ppmv during the convective event while a water vapour of 6 ppmv is found

Supprimé: in-situ ice

Supprimé: particle

Mis en forme : Anglais (États-Unis)

Supprimé: ed

481 above West Africa during the monsoon season by Khaykin et al. (2009). By comparison, convection
482 developing during the Asian monsoon over the Sichuan basin had a similar impact on the stratospheric water
483 budget as above West Africa. From the hourly budget of 869 t, we can also confirm that the local impact of
484 overshoots developed during the Asian summer monsoon is stronger than the one over tropical Africa
485 (300–500 t according to Liu et al., 2010) and is weaker than Hector the Convecteur over the Tiwi Islands
486 (2776 t according to Dauhut et al., 2015). Because of a large variety in the lifetime and horizontal scale of
487 overshoots, an accumulation of more event-scale analyses is important. In addition, note that the amount of
488 injected moisture is sensitive to the grid spacing of simulation, [\(up to a factor of 2 with horizontal grid](#)
489 [spacing varying from 1600 to 100 m; Dauhut et al., 2015\)](#) and the convection duration of target system. The
490 simple set up of tropospheric tracer of this study, i.e. tropospheric air below the 380 K isentropic altitude,
491 allows [the mixture of tropospheric and stratospheric air parcels in the TTL by vigorous convective](#)
492 [overshoots to be understood](#). To estimate the detailed origin i.e. defining the lower, middle, and upper
493 troposphere, of air parcel, further analyses [using passive tracers](#) (e.g. Mullendore et al., 2005; Hassim and
494 Lane, 2010; Homeyer, 2015; Dauhut et al., 2016) will be required. Also, additional numerical simulation
495 with a 2-moment microphysical scheme that considers mass and number concentration of hydrometeors and
496 aerosol together with options in the turbulent scheme (e.g., 1D against 3D formulation, Machado and
497 Chaboureau, 2015) will be worthwhile to study the impact on the results. To understand how much water
498 vapour and ice are generally injected into the TTL through convective overshoots during the Asian summer
499 monsoon is currently investigated in a follow-up study. Further, it would be interesting to investigate the
500 transport of chemical constituents, e.g. methane, nitrogen oxides, and carbon monoxide, via convective
501 overshoots during this season.

502 **Data availability**

503 [After the StratoClim embargo period, the aircraft data will be freely available. Meso-NH output data are](#)
504 [available from JPC upon request.](#)

505 **Author contribution**

506 KOL, TD and JPC designed the numerical simulation, and JPC performed the simulation. KOL, TD and JPC
507 designed the manuscript and analyses. SK provided the FLASH instrument data, and MK and CR provided

Supprimé: 3

Mis en forme : Police :Times New Roman, 11 pt, Anglais (États-Unis)

Mis en forme : Police :Times New Roman, 11 pt, Anglais (États-Unis)

Mis en forme : Police :Times New Roman, 11 pt, Anglais (États-Unis)

Mis en forme : Police :Times New Roman, 11 pt, Anglais (États-Unis)

Mis en forme : Police :Times New Roman, 11 pt, Anglais (États-Unis)

Supprimé: to understand

Supprimé: sophisticated passive tracer

Supprimé: r

Supprimé: Meso-NH output data are available from the authors upon request (keun-ok.lee@aero.obs-mip.fr or jean-pierre.chaboureau@aero.obs-mip.fr)

517 the FISH instrument data. KOL prepared the manuscript with contributions from all co-authors.

518

519 **Acknowledgement**

520 This study is funded by the StratoClim project by the European Union Seventh Framework Programme
521 under grant agreement no 603557 and the IDEX TEASAO project. Computer resources were allocated by
522 GENCI through project 90569.

523

524 **References**

525 Afchine, A., Rolf, C., Costa, A., Spelten, N., Riese, M., Buchholz, B., Ebert, V., Heller, R., Kaufmann, S.,
526 Minikin, A., Voigt, C., Zöger, M., Smith, J., Lawson, P., Lykov, A., Khaykin, S., and Krämer, M.: Ice
527 particle sampling from aircraft – influence of the probing position on the ice water content, Atmos.
528 Meas. Tech., 11, 4015–4031, <https://doi.org/10.5194/amt-11-4015-2018>, 2018.

529 Bougeault, P. and Lacarrère, P.: Parameterization of orography-induced turbulence in a meso-beta-scale
530 model. Mon. Weather Rev. 117(8): 1872–1890, <https://doi.org/10.1175%2F1520-0493%281989%29117%3C1872%3APOOITI%3E2.0.CO%3B2>, 1989.

531 Chaboureaud, J.-P., Cammas, J.-P., Duron, J., Mascart, P. J., Sitnikov, N. M., and Voessing, H. J.: A numerical
532 study of tropical cross-tropopause transport by convective overshoots, Atmos. Chem. Phys., 7, 1731–
533 1740, <https://doi.org/10.5194/acp-7-1731-2007>, 2007.

534 Chaboureaud, J.-P., and Coauthors: A midlatitude precipitating cloud database validated with satellite
535 observations. J. Appl. Meteor. Climatol., 47, 1337–1353, <https://doi.org/10.1175/2007JAMC1731.1>,
536 2008.

537 Chaboureaud, J.-P., and Coauthors: Long-range transport of Saharan dust and its radiative impact on
538 precipitation forecast: A case study during the Convective and Orographically-induced Precipitation
539 Study (COPS). Quart. J. Roy. Meteor. Soc., 137, 236–251, <https://doi.org/10.1002/qj.719>, 2011.

540 Colella, P. and Woodward, P. R.: The piecewise parabolic method (PPM) for gas dynamical simulations. J.
541 Comput. Phys. 54: 174–201, [https://doi.org/10.1016/0021-9991\(84\)90143-8](https://doi.org/10.1016/0021-9991(84)90143-8), 1984.

542 Cuxart, J., Bougeault, P., and Redelsperger, J. L.: A turbulence scheme allowing for mesoscale and large-
543 eddy simulations. Q. J. R. Meteorol. Soc. 126(562): 1–30, <https://doi.org/10.1002/qj.49712656202>,
544 2000.

Code de champ modifié

Mis en forme : Police :11 pt

Mis en forme : Police :(Par défaut) Times New Roman, 11 pt

Mis en forme : Police :(Par défaut) Times New Roman, 11 pt

Supprimé: doi:

Supprimé: :

548 Dauhut, T., Chaboureau, J. P., Escobar, J., and Mascart, P.: Large-eddy simulations of hector the convecteur
549 making the stratosphere wetter. *Atmos. Sci. Let.* 16, 135–140, <https://doi.org/10.1002/asl2.534>, 2015.

550 Dauhut, T., Chaboureau, J. P., Escobar, J., and Mascart, P.: Giga-LES of hector the convecteur and its two
551 tallest updrafts up to the stratosphere. *J. Atmos. Sci.*, 73, 5041–5060, <https://doi.org/10.1175/JAS-D-16-0083.1>, 2016.

552

553 Dauhut, T., Chaboureau, J. P., Haynes, P. H., and Lane, T. P.: The mechanisms leading to a stratospheric
554 hydration by overshooting convection. *J. Atmos. Sci.*, 75, 4383–4398, <https://doi.org/10.1175/JAS-D-18-0176.1>, 2018.

555

556 Dessler, A. E. and Sherwood, S. C.: Effect of convection on the summertime extratropical lower stratosphere,
557 *J. Geophys. Res.*, 109, D23301, <https://doi.org/10.1029/2004JD005209>, 2004.

558 Fueglistaler, S., Dessler, A. E., Dunkerton, T. J., Folkins, I., Fu, Q., and Mote, P. W.: Tropical tropopause
559 layer, *Rev. Geophys.*, 47, RG1004, <https://doi.org/10.1029/2008RG000267>, 2009.

560 Funatsu, B. M., Rysman, J. F., Claud, C., and Chaboureau, J. P.: Deep convective clouds distribution over the
561 Mediterranean region from AMSU-B/MHS observations, *Atmos. Res.*, 207, 122–135,
562 <https://doi.org/10.1016/j.atmosres.2018.03.003>, 2018.

563 Gal-Chen, T. and Somerville, R. C. J.: On the use of a coordinate transformation for the solution of the
564 Navier-Stokes equations. *J. Comput. Phys.* 17: 209–228, [https://doi.org/10.1016/0021-9991\(75\)90037-6](https://doi.org/10.1016/0021-9991(75)90037-6), 1975.

565

566 Homeyer, C. R., Pan, L. L., Dorsi, S. W., Avallone, L. M., Weinheimer, A. J., O'Brien, A. S., DiGangi, J. P.,
567 Zondlo, M. A., Ryerson, T. B., Diskin, G. S., and Campos, T. L.: Convective transport of water vapor
568 into the lower stratosphere observed during double-tropopause events. *J. Geophys. Res. Atmos.*, 119,
569 10941–10958, <https://doi.org/10.1002/2014JD021485>, 2014.

570 Homeyer, C. R.: Numerical simulations of extratropical tropopause penetrating convection, *J. Geophys. Res.*
571 *Atmos.*, 120, 7174–7188. <https://doi.org/10.1002/2015JD023356>, 2015.

572 Homeyer, C. R., McAuliffe, J. D., and Bedka, K. M.: On the development of above-anvil cirrus plumes in
573 Extratropical convection. *J. Atmos. Sci.*, 74, 1617–1633, <https://doi.org/10.1175/JAS-D-16-0269.1>,
574 2017

575 Hassim, M. E. E. and Lane, T. P.: A model study on the influence of overshooting convection on TTL water
576 vapour, *Atmos. Chem. Phys.*, 10, 9833–9849, <https://doi.org/10.5149/acp-10-9833-2010>, 2010.

Supprimé :

Supprimé: Accepted to

Supprimé: 2018.

Mis en forme : Police :(Par défaut) Times New Roman, 11 pt, Anglais (États-Unis)

Mis en forme : Police :(Par défaut) Times New Roman, 11 pt

Supprimé :

Supprimé :

Code de champ modifié

Mis en forme : Police :11 pt

Supprimé :

Supprimé :

Supprimé :

Code de champ modifié

Code de champ modifié

585 Highwood, E. J., and Hoskins, B. J.: The tropical tropopause, Q. J. R. Meteorol. Soc., 124, 1579–1604,
586 <https://doi.org/10.1002/qj.49712454911>, 1998.

587 Hoskins, B. J. and Rodwell, M. J.: A model of the Asian summer monsoon, I, The global scale, J. Atmos. Sci.,
588 52, 1329–1340, [https://doi.org/10.1175/1520-
589 0469%281995%29052%3C1329%3AAMOTAS%3E2.0.CO%3B2](https://doi.org/10.1175/1520-0469%281995%29052%3C1329%3AAMOTAS%3E2.0.CO%3B2), 1995.

590 Jensen, E., Ackerman, A. S. and Smith, J. A.: Can overshooting convection dehydrate the tropical tropopause
591 layer? J. Geophys. Res., 112, D11209, <https://doi.org/10.1029/2006JD007943>, 2007.

592 Kato T.: Structure of the band-shaped precipitation system inducing the heavy rainfall observed over
593 northern Kyushu, Japan on 29 June 1999. J. Meteor. Soc. Japan. 84,129–153,
594 <https://doi.org/10.2151/jmsj.84.129>, 2006.

595 Khaykin, S. M., Pommereau, J.-P., Riviere, E. D., Held, G., Ploeger, F., Gysels, M., Amarouches, N., Vernier,
596 J.-P., Wienhold, F. G., and Ionov, D.: Evidence of horizontal and vertical transport of water in the
597 southern hemisphere tropical tropopause layer (TTL) from high-resolution balloon observation,
598 Atmos. Chem. Phys., 16, 12273–12286, <https://doi.org/10.5194/acp-16-12273-2016>, 2016.

599 Khaykin, S., Pommereau, J.-P., Korshunov, L., Yushkov, V., Nielsen, J., Larsen, N., Christense, T., Garnier,
600 A., Lukyanov, A., and Williams, E.: Hydration of the lower stratosphere by ice crystal geysers over
601 land convective systems, 9, 2275–2287, <https://doi.org/10.5194/acp-9-2275-2009>, 2009.

602 Khaykin, S. M., Engel, I., Vömel, H., Formanyuk, I. M., Kivi, R., Korshunov, L. I., Krämer, M., Lykov, A.
603 D., Meier, S., Naebert, T., Pitts, M. C., Santee, M. L., Spelten, N., Wienhold, F. G., Yushkov, V. A., and
604 Peter, T.: Arctic stratospheric dehydration – Part 1: Unprecedented observation of vertical
605 redistribution of water, Atmos. Chem. Phys., 13, 11503–11517, [https://doi.org/10.5194/acp-13-11503-
606 2013](https://doi.org/10.5194/acp-13-11503-2013), 2013.

607 Lac, C., Chaboureaud, J. P., Masson, V., Pinty, J. P., Tulet, P., Escobar, J., Leriche, M., Barthe, C., Aouizerats,
608 B., Augros, C., Aumond, P., Auguste, F., Bechtold, P., Berthet, S., Bieilli, S., Bosseur, F., Caumont, O.,
609 Cohard, J. M., Colin, J., Couvreur, F., Cuxart, J., Delautier, J., Dauhut, T., Ducrocq, V., Filippi, J.B.,
610 Gazen, D., Geoffroy, O., Gheusi, F., Honnert, R., Lafore, J. P., Lebeaupin, Brossier C., Libois, Q.,
611 Lunet, T., Mari, C., Maric, T., Mascart, P., Mogé, M., Molinié, G., Nuissier, O., Pantillon, F., Peyrillé,
612 P., Pergaud, J., Perraud, E., Pianezze, J., Redelsperger, J. L., Ricard, D., Richard, E., Riette, S., Rodier,
613 Q., Schoetter, R., Seyfried, L., Stein, J., Suhre, K., Taufour, M., Thouron, O., Turner, S., Verrelle, S.,

Code de champ modifié

Mis en forme : Français (France)

Mis en forme : Lien hypertexte, Police : (Par défaut) Liberation Serif, 12 pt, Couleur de police : Couleur personnalisée(RVB(0;0;10)), Français (France)

Mis en forme : Lien hypertexte, Police : (Par défaut) Liberation Serif, 12 pt, Couleur de police : Couleur personnalisée(RVB(0;0;10)), Français (France)

Code de champ modifié

Mis en forme : Français (France)

Supprimé :

Code de champ modifié

Code de champ modifié

Code de champ modifié

615 Vié, B., Visentin, F., Vionnet, V., and Wautelet, P.: Overview of the Meso-NH model version 5.4 and
616 its applications. *Geosci. Model Dev.*, 11, 1929–1969, <https://doi.org/10.5194/gmd-11-1929-2018>, 2018.

617 Lee, K. O., Flamant, C., Ducrocq, V., Duffourg, F., Fourrié, N., and Davolio, S. : Convective initiation and
618 maintenance processes of two back-building mesoscale convective systems leading tow heavy
619 precipitation events in South Italy during HyMeX IOP 13. *Q. J. R. Meteorol. Soc.*, 142, 2623–2635,
620 <https://doi.org/10.1002/qj.2851>, 2016.

621 Liu, C., and Zipser, E. J.: Global distribution of convection penetrating the tropical tropopause, *J. Geophys.*
622 *Res.*, 110, D23104, <https://doi.org/10.1029/2005JD006063>, 2005.

623 Liu, X. M., Rivière, E. D., Marécal, V., Durry, G., Hamdouni, A., Arteta, J., and Khaykin, S.: Stratospheric
624 water vapour budget and convection overshooting the tropopause: modelling study from SCOUT-
625 AMMA. *Atmos. Chem. Phys.*, 10, 8267–8286, www.atmos-chem-phys.net/10/8267/2010, 2010.

626 Machado, L. A., and Chaboureau, J. P.: Effect of Turbulence Parameterization on Assessment of Cloud
627 Organization. *Mon. Wea. Rev.*, 143, 3246–3262, <https://doi.org/10.1175/MWR-D-14-00393.1>, 2015.

628 Maddox, E. M. and Mullendore, G. L.: Determination of best tropopause definition for convective
629 transportation studies. *J. Atmos. Sci.*, 75, 3433–3446, <https://doi.org/10.1175/JAS-D-18-0032.1>, 2018.

630 Mason, R. and Anderson, C.: The development and decay of the 100-MB. Summertime anticyclone over
631 southern Asia. *Mon. Wea. Rev.*, 1, 3–12, [https://doi.org/10.1175/1520-](https://doi.org/10.1175/1520-0493%281963%29091%3C0003%3ATDADOT%3E2.3.CO%3B2)
632 [0493%281963%29091%3C0003%3ATDADOT%3E2.3.CO%3B2](https://doi.org/10.1175/1520-0493(1992)120%3C0003%3ATDADOT%3E2.3.CO%3B2), 1963.

633 Meyer, J., Rolf, C., Schiller, C., Rohs, S., Spelten, N., Afchine, A., Zöger, M., Sitnikov, N., Thornberry, T. D.,
634 Rollins, A. W., Bozóki, Z., Tátrai, D., Ebert, V., Kühnreich, B., Mackrodt, P., Möhler, O., Saathoff, H.,
635 Rosenlof, K. H., and Krämer, M.: Two decades of water vapor measurements with the FISH
636 fluorescence hygrometer: a review, *Atmos. Chem. Phys.*, 15, 8521–8538, [https://doi.org/10.5194/acp-](https://doi.org/10.5194/acp-15-8521-2015)
637 [15-8521-2015](https://doi.org/10.5194/acp-15-8521-2015), 2015.

638 Mullendore, G. L., Durran, D. R., and Holton, J. R.: Cross-Tropopause tracer transport in midlatitude
639 convection, *J. Geophys. Res.*, 110, D06113, <https://doi.org/10.1029/2004JD005059>, 2005.

640 Müller R.: The performance of classical versus modern finite-volume advection schemes for atmospheric
641 modelling in a one-dimensional test-bed. *Mon. Wea. Rev.*, 120, 1407–1415,
642 [https://doi.org/10.1175/1520-0493\(1992\)120%3C1407:TPOCV%3E2.0.CO;2](https://doi.org/10.1175/1520-0493(1992)120%3C1407:TPOCV%3E2.0.CO;2), 1992.

643 Park, M., Randel, W. J., Kinnison, E. J., Garcia, R. R., and Choi, W.: Seasonal variation of methane, water

Code de champ modifié

Supprimé :

Mis en forme : Police :(Par défaut) Times New Roman, 11 pt

Mis en forme : Police :11 pt

Code de champ modifié

Mis en forme : Police :11 pt

Code de champ modifié

Code de champ modifié

Supprimé :

Code de champ modifié

646 vapor and nitrogen oxides near the tropopause: Satellite observations and model simulation, J.
647 Geophys. Res., 109, D03302, <https://doi.org/10.1029/2003JD003706>, 2004.

648 Pinty, J. P. and Jabouille, P.: A mixed-phased cloud parametrization for use in a mesoscale non-hydrostatic
649 model: Simulations of a squall line and of orographic precipitation. In: Proc. Of the Conference on
650 Cloud Physics. Amer. Meteorol. Soc, Boston: Everett, WA, USA, 17–21 Aug. 1998. Pp. 217–220,
651 1998.

652 Randel, W. J. and Park, M.: Deep convective influence on the Asian summer monsoon anticyclone and
653 associated tracer variability observed with Atmospheric Infrared Sounder (AIRS), J. Geophys. Res.,
654 111, D12314, <https://doi.org/10.1029/2005JD006490>, 2006.

655 Randel, W. J., Wu, F., Gettelman, A., Russell, J. M., Zawodny, J. M., and Oltmans, S. J.: Seasonal variation
656 of water vapour in the lower stratosphere observed in Halogen Occultation Experiment data, J.
657 Geophys. Res., 106(D13), 14313–14325, <https://doi.org/10.1029/2001JD900048>, 2001.

658 Rysman, J. F., Claud, C., Chaboureau, J. P., Delanoë, J., and Funatsu, B. M.: Severe convection in the
659 Mediterranean from microwave observations and a convection-permitting model, Quart. J. Roy.
660 Meteor. Soc., 142, 43–55, <https://doi.org/10.1002/qj.2611>, 2016.

661 Rolf, C., Vogel, B., Hoor, P., Afchine, A., Günther, G., Krämer, M., Müller, R., Müller, S., Spelten, N., and
662 Riese, M.: Water vapor increase in the lower stratosphere of the northern hemisphere due to the Asian
663 monsoon anticyclone observed during the TACTS/ESMVal campaigns, Atmos. Chem. Phys., 18,
664 2973–2983, <http://doi.org/10.5194/acp-18-2973-2018>, 2018.

665 Saunders, R., Hocking, J., Rundle, D., Rayer, P., Matricardi, M., Geer, A., Lupu, C., Brunel, P., and Vidot, J.:
666 RTTOV-11—Science and validation report. NWP SAF Tech. Rep., 62 pp., 2013.

667 Shu, C. W. and Osher, S.: Efficient implementation of essentially non-oscillatory shock-capturing schemes.
668 Journal of Computational Physics 77(2): 439–471, [https://doi.org/10.1016/0021-9991\(88\)90177-5](https://doi.org/10.1016/0021-9991(88)90177-5),
669 1988.

670 Sitnikov, N. M., Yushkov, V. A., Afchine, A. A., Korshunov, L. I., Astakhov, V. I., Elanovskii, A. E., Kraemer,
671 M., Mangold, A., Schiller, C., and Ravegnani, F.: The FLASH instrument for water vapor
672 measurements on board the high-altitude airplane. Instrum. Exp. Tech., 50, 113–121,
673 <https://doi.org/10.1134/S0020441207010174>, 2007.

674 Smith, J. B., Wilmouth, D. M., Bedka, K. M., Bowman, K. P., Homeyer, C. R., Dykema, J. A., Sargent, M.

Supprimé :

Supprimé :

Code de champ modifié

Mis en forme : Police :(Par défaut) Times New Roman, 11 pt

Mis en forme : Police :11 pt

Code de champ modifié

Code de champ modifié

Code de champ modifié

677 R., Clapp, C. E., Leroy, S. S., Sayres, D. S., Dean-Day, J. M., Bui, T. P., and Anderson, J. G.: A case
678 study of convectively sourced water vapor observed in the overworld stratosphere over the United
679 States. *J. Geophys. Res.*, 122, 9529–9554, <https://doi.org/10.1002/2017JD026831>, 2017.

680 Tissier, A.-S. and Legras, B.: Convective sources of trajectories traversing the tropical tropopause layer.
681 *Atmos. Chem. Phys.*, 16, 3383–3398, <https://doi.org/10.5194/acp-16-3383-2016>, 2016.

682 Tzella, A. and Legras, B.: A Lagrangian particle dispersion model FLEXPART version 6.2. *Atmos. Chem.*
683 *Phys.*, 5, 2461–2474, <https://doi.org/10.5194/acp-5-2461-2005>, 2005.

684 Winker, D. M., Vaughan, M. A., Omar, A., Hu, Y., Powell, K. A., Liu, Z., Hunt, W. H., and Young, S. A.:
685 Overview of the CALIPSO mission and CALIOP data processing algorithms. *J. Atmos. Oceanic*
686 *Technol.*, 26, 2310–2323, <https://doi.org/10.1175/2009JTECHA1281.1>, 2009.

687 WMO: Definition of the tropopause, *WMO Bull.*, 6, 136, 1957.

688 Wright, J. S., Fu, R., Fueglistaler, S., Liu, Y. S., and Zhang, Y.: The influence of summertime convection over
689 Southeast Asia on water vapor in the tropical stratosphere. *J. Geophys. Res.*, 116, D12302,
690 <https://doi.org/10.1029/2010JD015416>, 2011.

691 Zöger, M., Afchine, A., Eicke, N., Gerhards, M.-T., Klein, E., McKenna, D., Mörschel, U., Schmidt, U., Tan,
692 V., Tuitjer, F., Woyke, T., and Schiller, C.: Fast in situ stratospheric hygrometers: A new family of
693 balloon-borne and airborne Lyman-photofragment fluorescence hygrometers, *J. Geophys. Res.*, 104,
694 1807–1816, <https://doi.org/10.1029/1998JD100025>, 1999.

695

Supprimé :

Code de champ modifié

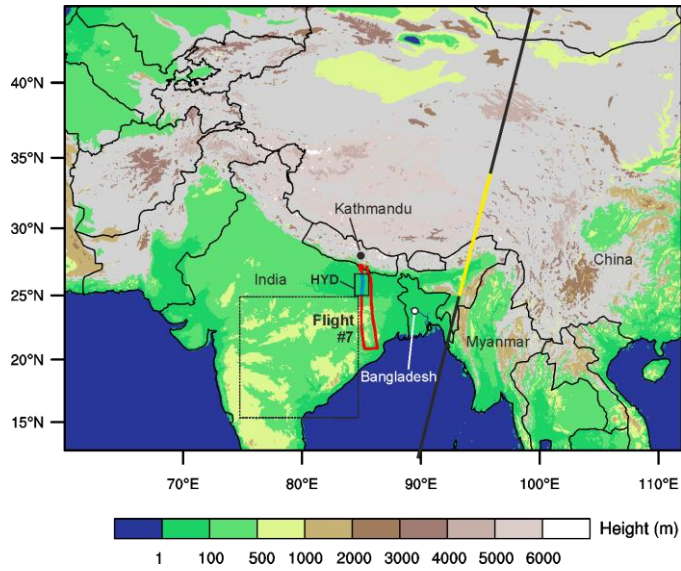
Supprimé :

Mis en forme : Police :(Par défaut) Times New Roman,
11 pt

Supprimé :

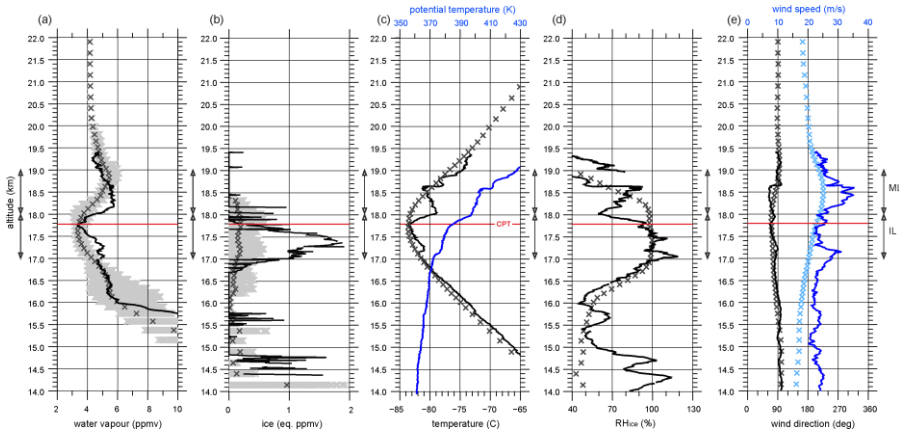
Supprimé :

Code de champ modifié

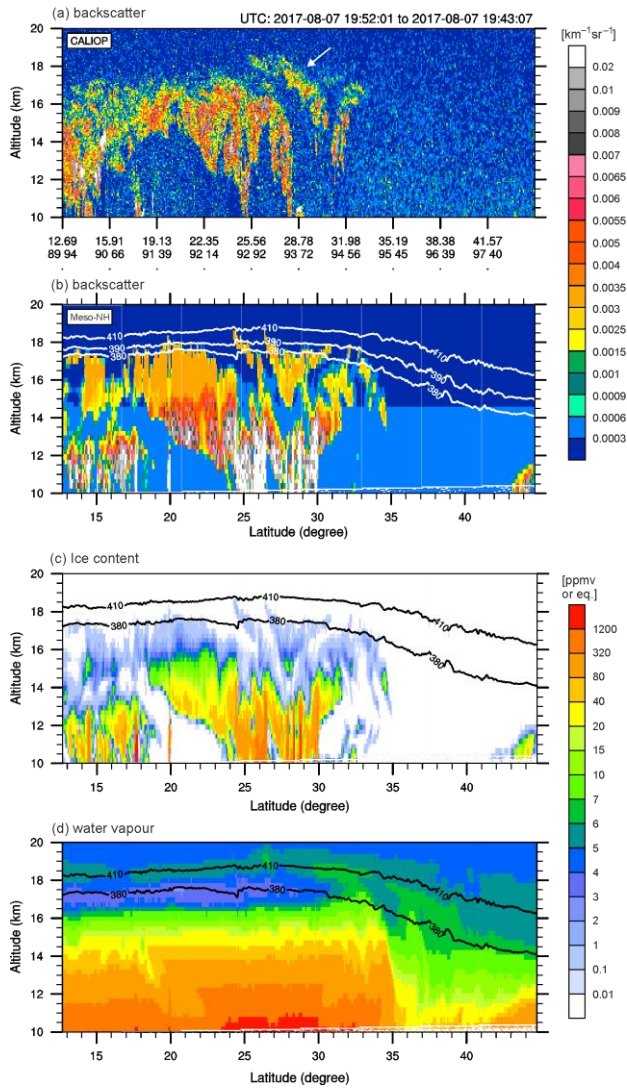


700
701
702
703
704
705
706
707

Figure 1. Topography and domain considered in the Meso-NH numerical simulation with a resolution of 2.5 km. The trajectory of the Geophysica flight #7 to the south of Kathmandu is shown by the red solid line, while the pathway of moist patch (25–26.5°N) is depicted by the blue line. A black box ‘HYD’ is a model domain considered in comparison with aircraft measurement. Another box with dashed line is a model domain used to calculate the background water vapour at 06:00 UTC on 8 August 2017. The track of CALIOP around 20:00 UTC on 7 August 2017 is shown by the black solid line while its track between 25 and 33°N is highlighted in yellow.

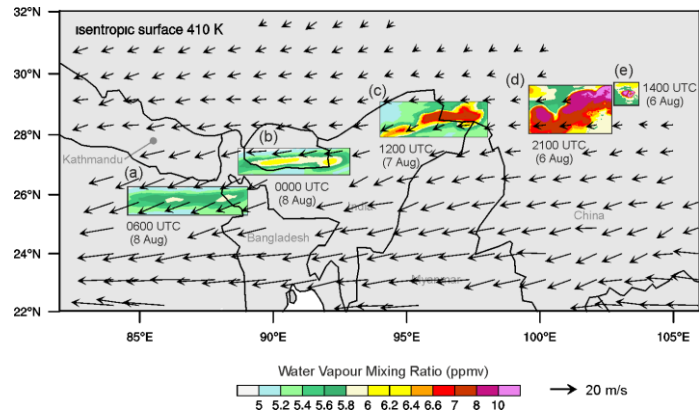


708
 709 **Figure 2.** Vertical profiles of (a) water vapour (ppmv), (b) ice (eq. ppmv), (c) temperature ($^{\circ}\text{C}$) and potential temperature (K), (d)
 710 relative humidity respect to ice (RH_{ice} , %), and (e) wind direction (degree) and speed (m s^{-1}). In (a)–(e), the measured values along
 711 the blue-coloured track between $25\text{--}26.5^{\circ}\text{N}$ (shown in Fig. 1) from 06:20 to 06:48 UTC on 8 August 2017 are shown as solid line,
 712 while the domain averaged values in the region ‘HYD’ ($25\text{--}26.5^{\circ}\text{N}$, $85\text{--}85.5^{\circ}\text{E}$, shown in Fig. 1) from the Meso-NH simulation at
 713 06:00 UTC on the same day are shown as cross marks. In (a)–(e), the level of cold point tropopause (CPT) is indicated by a red line.
 714 In (a)–(b), all the values from Meso-NH within the ‘HYD’ is displayed by grey cross marks. The layers of ML and IL are marked by
 715 arrows.



716
 717 **Figure 3.** Backscatters at 532 nm (a) measured by CALIOP around 20:00 UTC and (b) retrieved by the Meso-NH simulation, and (c)
 718 ice content (eq. ppmv) and (d) water vapour (ppmv) produced by the Meso-NH simulation along the CALIOP track (marked by solid
 719 line in Fig. 1) at 20:00 UTC on 7 August 2017.

720

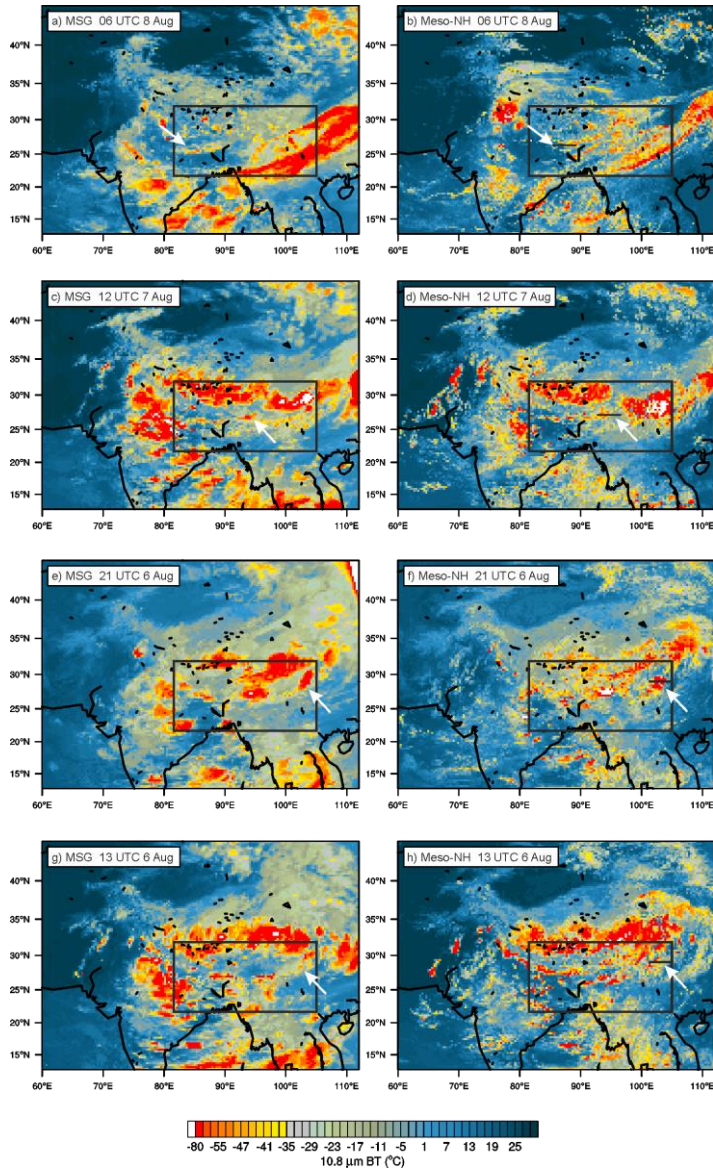


721

722 **Figure 4.** Target moist patch. Horizontal distribution of water vapour mixing ratio at 410 K isentropic altitude at (a) 06:00 UTC, and

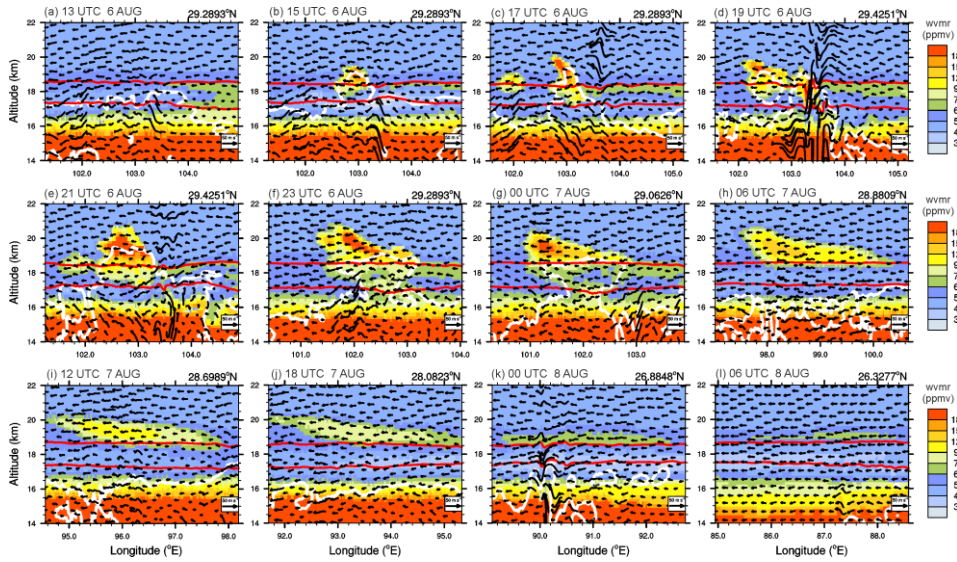
723 (b) 00:00 UTC on 8 August, (c) 12:00 UTC on 7 August, (d) 21:00 UTC and (e) 14:00 UTC on 6 August 2017. The horizontal wind

724 at the altitude of 19 km (about 410 K isentrope) at 06:00 UTC on 8 August is displayed by vectors.



725

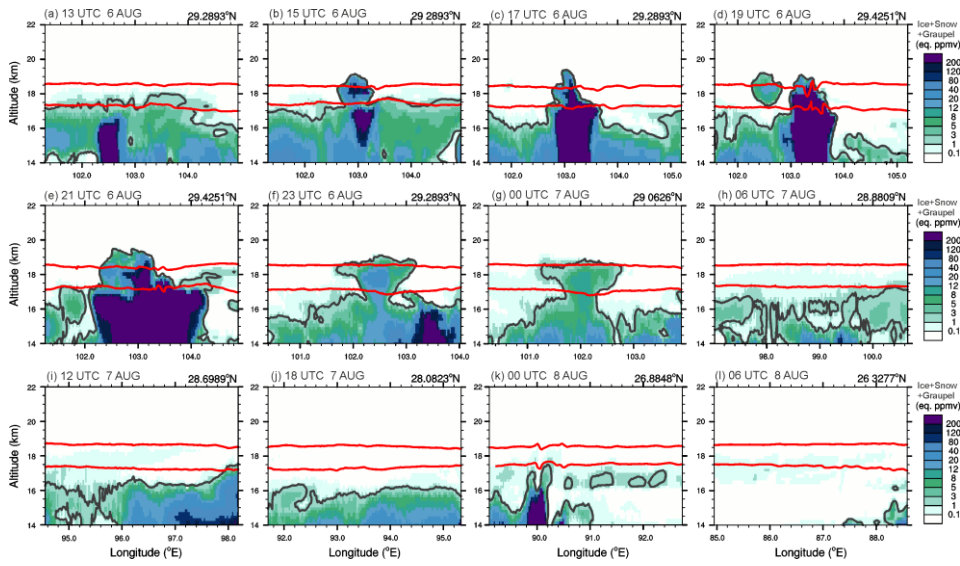
726 **Figure 5.** BT 10.8 μm obtained from SEVIRI/MSG (left) and Meso-NH (right) at (a)–(b) 06:00 UTC on 8 August, (c)–(d) 12:00
 727 UTC on 7 August, (e)–(f) 21:00 UTC, and (f)–(h) 13:00 UTC on 6 August 2017. The domain used in Figure 4 is marked by a box in
 728 each panel, while the location of vertical cross-sections used in Figures 6–9 is marked by a black solid line in the right panels. The
 729 location of hydration patch is depicted by the white arrows.



730
731

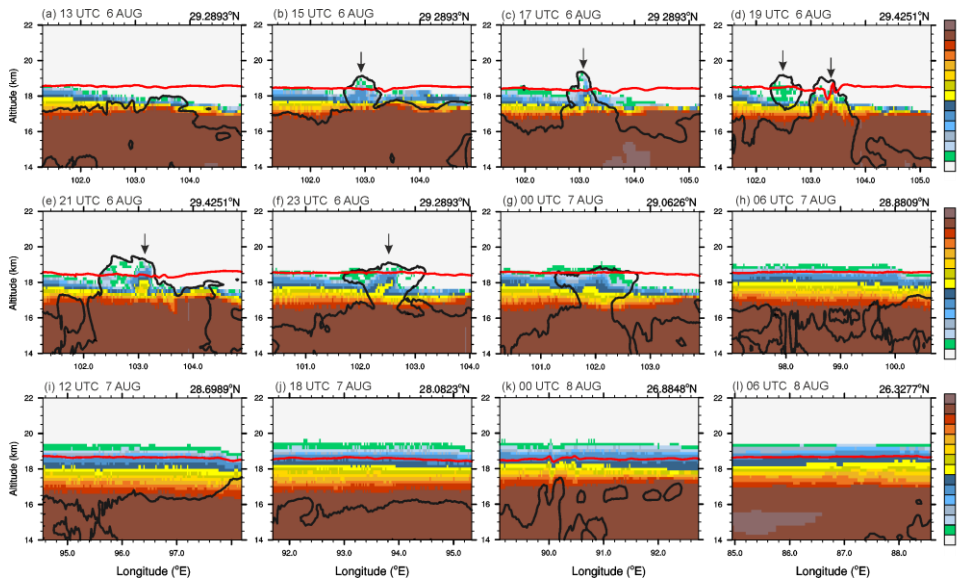
732 **Figure 6.** Vertical cross-sections of water vapour mixing ratio (shading) and wind (vectors) (a) 13:00 UTC, (b) 15:00 UTC, (c) 17:00
733 UTC, (d) 19:00 UTC, (e) 21:00 UTC, (f) 23:00 UTC on 6 August 2017, (g) 00:00 UTC, (h) 06:00 UTC, (i) 12:00 UTC, (j) 18:00
734 UTC on 7 August 2017, and (k) 00:00 UTC and (l) 06:00 UTC on 8 August 2017. The isentropic altitudes of 380 and 410 K are
735 depicted by the red lines. The latitude (°N) of west-east oriented cross-section line is indicated at the upper right of each panel. The
736 cloud boundary (mixing ratio of ice content of 10 mg kg^{-1}) is contoured by the white solid line.

737



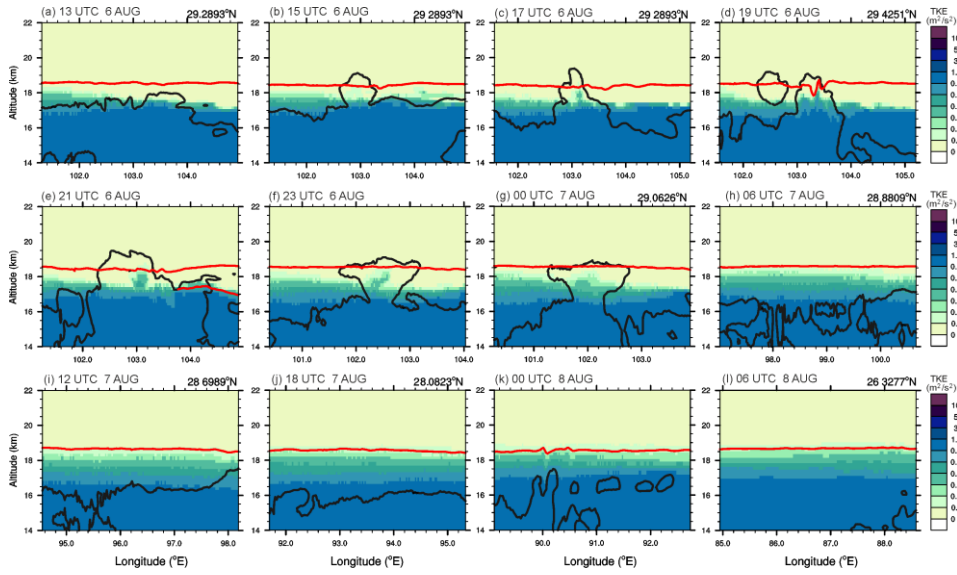
738
739
740
741
742

Figure 7. Same as Fig. 6 but for the ice content. The isentropic altitudes of 380 and 410 K are depicted by the red lines.



743
744
745
746

Figure 8. Same as Fig. 6 but for the tracer (%). The isentropic altitude of 410 K is depicted by the red line. The changes of the tropospheric tracer by convective overshoots is marked by downward arrows.



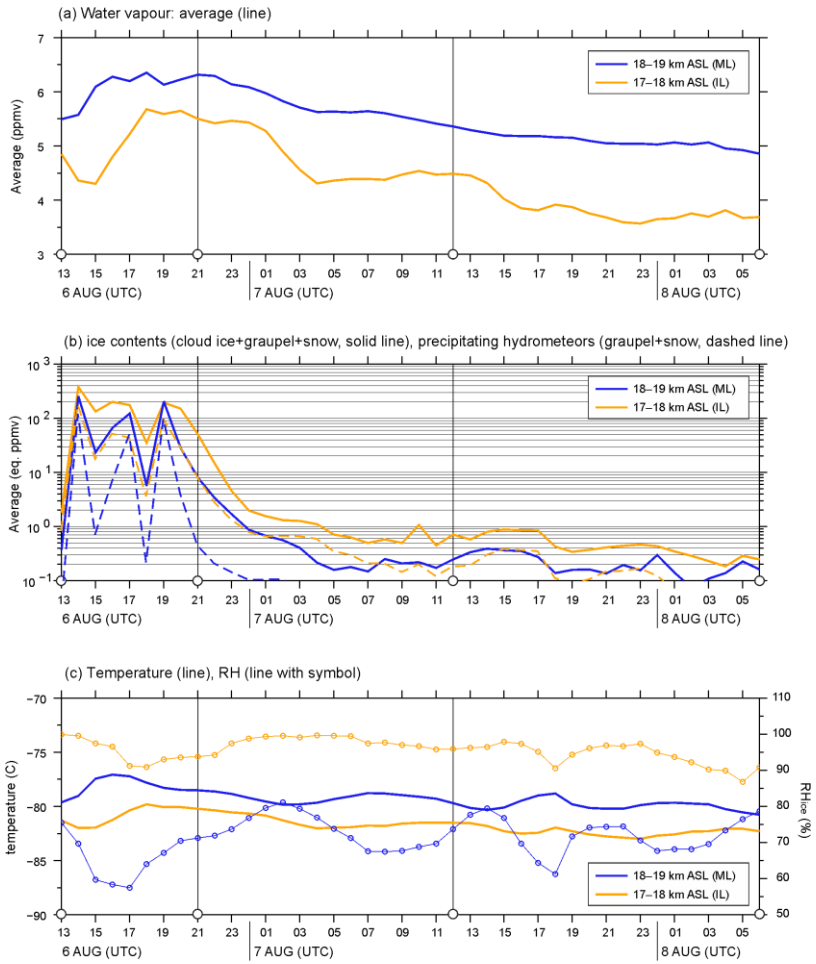
747

748

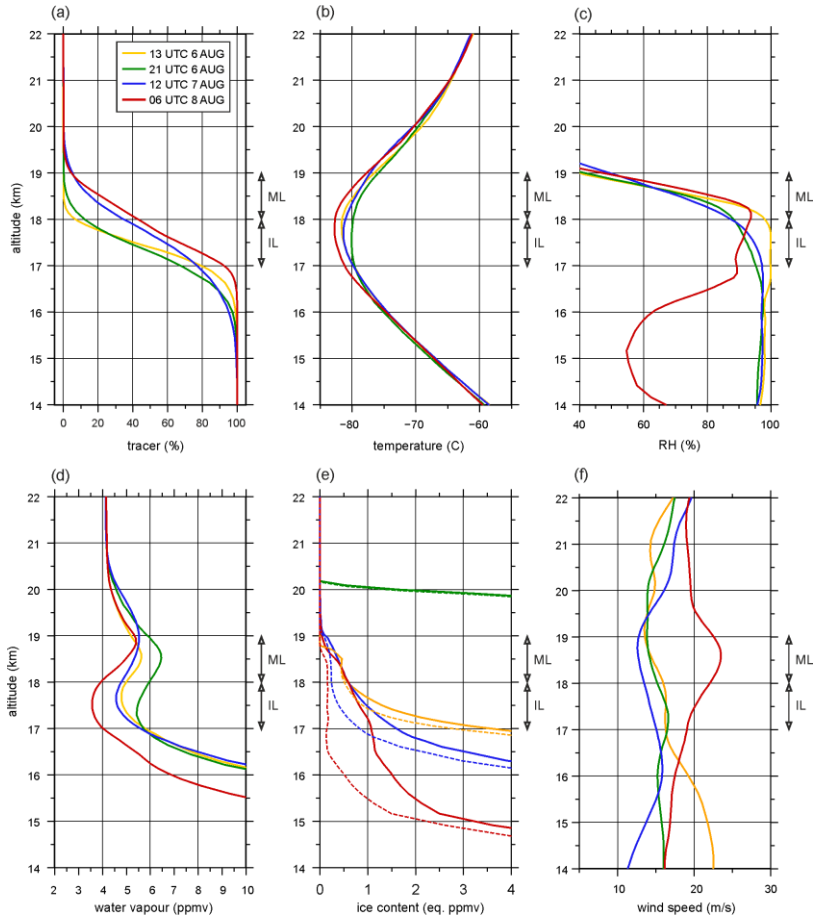
749

Figure 9. Same as Fig. 6 but for the TKE. The isentropic altitude of 410 K is depicted by the red line.

750

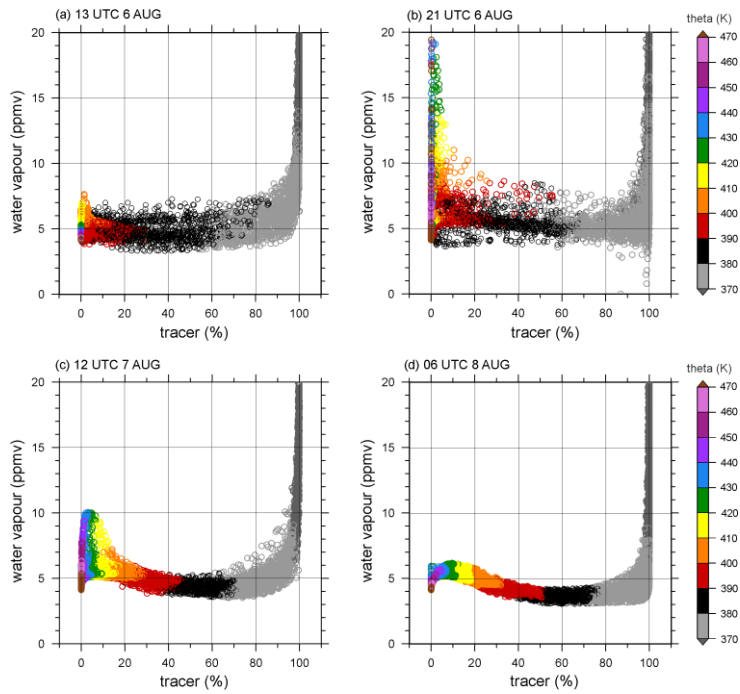


751
 752 **Figure 10.** Hourly evolution of (a) averaged water vapour (line), (b) averaged ice content (solid line, sum of ice, graupel, and snow)
 753 and the precipitating hydrometeor (dashed line, sum of graupel and snow), and (c) averaged temperature (line) and relative humidity
 754 (RH_{ice} , thin line with circle) in the altitudes of 17–18 km (yellow lines) and 18–19 km (blue lines) ASL from 13:00 UTC on 6 August
 755 to 06:00 UTC on 8 August 2017. The four analysis times are marked by open circles on the x-axis. Average and maximum values are
 756 calculated in ML and IL.
 757



758

759 **Figure 11.** Vertical profiles of (a) tracer (%), (b) temperature ($^{\circ}\text{C}$), (c) relative humidity (%), mixing ratios of (d) water vapour
 760 (ppmv), (e) ice content (eq. ppmv), and (f) wind speed (m s^{-1}) across the hydration patch along the trajectory at 13:00 UTC (yellow
 761 line), 21:00 UTC (green line) on 6 August, 12:00 UTC on 7 August (blue line), and 06:00 UTC (red line) on 8 August 2017. The
 762 layers of ML and IL are marked by arrows. In (e), the ice content is depicted by solid lines, while the cloud ice are shown by
 763 dashed lines.

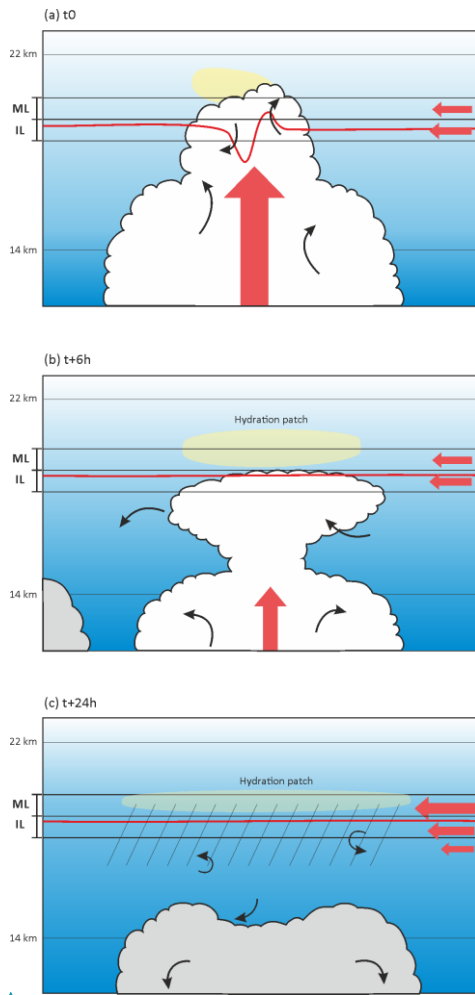


764

765 **Figure 12.** Mixing diagram using tropospheric tracer (%) and water vapour (ppmv) across the hydration patch in the altitudes

766 between 14 and 22 km ASL along the trajectory at (a) 13:00 UTC on 6 August, (b) 21:00 UTC on 6 August, (c) 12:00 UTC on 7

767 August, and (d) 06:00 UTC on 8 August 2017. The potential temperature (K) is shown with colour shading.



768
769

770 **Figure 13.** Schematic illustration summarising the hydration process in the TTL during flight #7 of the StratoClim 2017 field
 771 campaign. (a) Mixing of the overshoots with the stratospheric air, (b) and (c) turbulent mixing of the hydration patch with the
 772 tropospheric air by vertical wind shear. The bottom and top of the TTL, 14 and 22 km, and the moist layer (ML) and ice layer (IL) are
 773 represented by the black solid line, and the 410 K isentropic altitude is represented by the red solid line. The main force in the TTL is
 774 marked by bold red arrows, while the turbulent eddies in/around the developed and weakened overshoots are described by black
 775 arrows. The overreaching water vapour above the cloud top level is indicated by a yellow ellipsoid in (a). The hydration patch is
 776 yellow-encapsulated in (a) and (b), and the layer of dehydration by turbulent diffusion and [water vapour deposition followed by ice](#)
 777 [sedimentation](#) is hatched in (c). The blue shades illustrate the concentration of tropospheric air, showing the increased tropospheric
 778 air in the TTL by the turbulent mixing in (b) and (c).

Mis en forme : Police :(Par défaut) Times New Roman, 9 pt, Gras

Supprimé: microphysics

Supprimé: